Evaluation of polyol-made Gd3+ -substituted Co0.6Zn0.4Fe2O4 nanoparticles as high magnetization MRI negative contrast agents

Walid Mnasri, Lotfi Bentahar, Sophie Nowak, Olivier Sandre, Michel Boissière, Souad Ammar

Journal of Interdisciplinary Nanomedicine

BRITISH SOCIETY FOR NANOMEDICINE

Open Access

Journal of Interdisciplinary Nanomedicine ISSN 2058-3273

ORIGINAL ARTICLE

Evaluation of polyol-made Gd^{3+}-substituted $Co_{0.6}Zn_{0.4}Fe_2O_4$ nanoparticles as high magnetization MRI negative contrast agents

Walid Mnasri,[1,2,3,4] Lotfi Bentahar,[2,5] Sophie Nowak,[1] Olivier Sandre,[4] Michel Boissière[3] & Souad Ammar[1*]

[1] *Sorbonne Paris Cité, Laboratoire Interface Traitement Organisation et DYnamique des Systèmes (ITODYS), CNRS UMR-7086, Université Paris Diderot, Paris75205, France*

[2] *Faculté des Sciences de Bizerte, Laboratoire Synthèse et Structures des Nanomatériaux UR11ES30, Université de Carthage, Jarzouna7021, Tunisia*

[3] *Maison Internationale de la Recherche, Laboratoire ERRMECe, Université de Cergy-Pontoise, Neuville sur Oise95031, France*

[4] *Bordeaux INP, Laboratoire de Chimie des Polymères Organiques (LCPO), CNRS UMR-5629, Université de Bordeaux, Pessac33600, France*

[5] *Faculty of Science of Arar, Northern Border University, P.O. Box 1231, Arar91431, Saudi Arabia*

Keywords
Gadolinium-substituted cobalt-zinc ferrite, MRI negative contrast agents, nanoparticles, polyol process.

Correspondence
Souad Ammar, Sorbonne Paris Cité, Laboratoire Interface Traitement Organisation et DYnamique des Systèmes (ITODYS), CNRS UMR-7086, Université Paris Diderot, Paris 75205, France.
Tel: +33 157278762;
Fax: +33 157277263;
E-mail: ammarmer@univ-paris-diderot.fr

FUNDING INFORMATION
ANR (Agence Nationale de la Recherche) (ANR 11 IDEX 05 02, ANR 11 LABX 086)

Received: 28 July 2018;
Revised: 17 October 2018;
Accepted: 12 November 2018

Journal of Interdisciplinary Nanomedicine, 2019; 4(1), doi: 10.1002/jin2.53

Abstract

The structural, microstructural, and magnetic properties of ~5-nm-sized $Co_{0.6}Zn_{0.4}Fe_{2-x}Gd_xO_4$ nanoparticles were investigated in order to evaluate their capability to enhance the magnetic resonance imaging contrast as high magnetization agents. A focus was made on the solubility of Gd^{3+} cations within the spinel lattice. By coupling X-ray diffraction to X-ray fluorescence spectroscopy, we demonstrated that only a limited fraction of Gd^{3+} can substitute Fe^{3+} ions into the whole crystal structure and does not exceed 6 at.-%. At this concentration, the room temperature (27°C) saturation magnetizations of the prepared superparamagnetic nanocrystals were found to be close to 80 emu g^{-1}. Coating these nanoparticles with hydrophilic dopamine ligands leads to the formation of ~50-nm-sized clusters in water. As a consequence, relatively high r_2/r_1 ratios of transverse to longitudinal proton relaxivities and high r_2 values were measured in the resulting colloids at physiological temperature (37°C) for an applied magnetic field of 1.41 T: 33 and 188 mM^{-1} sec^{-1}, respectively, for the richest system in gadolinium. Moreover, after incubation with healthy human model cells (fibroblasts) at doses as high as 10 μg mL^{-1}, they induce neither cellular death nor acute cellular damage making the engineered probes particularly valuable for negative magnetic resonance imaging contrasting.

Introduction

Superparamagnetic iron oxide nanoparticles (SPIONs) are largely used as negative contrast agents for magnetic resonance imaging (MRI), because of their ability to shorten the longitudinal T_1 and transversal T_2 relaxation times of the nuclear magnetic moment of water protons. According to the model of Gillis et al. (1999) named "Outer Sphere" mechanism, the increase in the relaxation rate $1/T_2$ compared with pure water originates from fluctuating dipolar interactions between nuclear spins of water protons and the electronic magnetic moment of SPIONs. This increase is as important as the transversal relaxivity, r_2, of SPIONs, defined as the slope of the variation of $1/T_2$ as a function of the iron atom concentration, is high, and then as the contrasting efficiency is improved. Vuong et al. (2012) have shown that r_2 follows a universal scaling law that is quadratic both with the volume magnetization and with the radius of the outer sphere, d, also called the relaxometric size: d is defined as the minimum approach distance between H_2O molecules and the SPIONs and very often approximated with the hydrodynamic diameter of the particles. They defined two limit water diffusion regimes, depending on the magnetic contrast agent characteristics. The first one is called the "motional averaging regime" (MAR), for which the protons of freely diffusing water molecules surrounding the particle explore all the possible values of magnetic dipolar field created by the SPIONs. The second one is called the "static dephasing regime" (SDR), for which, during one echo time of the applied radiofrequency sequence, water molecules explore only a small space compared with the hydrodynamic particle volume. In these regimes, the r_2 relaxivity can be expressed as follows, where equation 1a is related to the MAR and equation 1b to the SDR:

$$r_2 = \frac{R_2}{[\mathrm{Fe}]} = \frac{4\gamma^2\mu_0^2 v_{\mathrm{mat}} M_v^2 d^2}{405D}, \quad (1a)$$

$$r_2^* = \frac{R_2^*}{[\mathrm{Fe}]} = \frac{2\pi\gamma\mu_0 v_{\mathrm{mat}} M_v}{9\sqrt{3}} \approx r_2, \quad (1b)$$

where D measures the water translational diffusion constant (D = $3\cdot10^{-9}$ m^2 sec^{-1} at 37°C; Solomon, 1955; Bloembergen and Morgan, 1961), v_{mat} is the iron oxide molar volume defined by the ratio of the molar mass divided by the number of magnetic ions in the formula unit and by the mass density (v_{mat} = $1.56\cdot10^{-5}$ and $1.49\cdot10^{-5}$ m^3 mol^{-1} for maghemite and magnetite, respectively), μ_0 corresponds to the magnetic permeability of vacuum ($\mu_0 = 4\pi\cdot10^{-7}$ T m A^{-1}), and γ is the gyromagnetic factor of proton (γ = $2.67513\cdot10^8$ rad sec^{-1} T^{-1}). The transition between the two regimes is determined by the so-called Redfield condition (Vuong et al., 2012), in which $\Delta\omega$ = (1/3) ($\gamma\mu_0 M_v$) is the angular frequency shift experienced by a water proton, at the closest distance to the particle surface, and τ_D = $d^2/4D$ measures the translational diffusion time of a water molecule around the SPION sphere:

$\Delta\omega\cdot\tau_D < 1$ means the predominance of the MAR regime, while $\Delta\omega\cdot\tau_D > 1$ means the predominance of the SDR regime.

The first regime (MAR) is the most common for small single nanoparticles (NPs) of pure magnetic materials or with a thin fully hydrated shell and for hybrid entities whose overall magnetization M_v (the total magnetic moment divided by the particle volume) remains small compared with the specific magnetization of their inorganic part (m_S). In that case, the magnetic cores are either dispersed individually or clustered yet wrapped by a rather thick coating (silica, polymer) impermeable to water (thus, the magnetization is averaged over the whole outer sphere diameter instead of just the magnetic core). According to this model, the design of powerful negative contrast agents for MRI is dictated by three parameters only: the intrinsic magnetization of their constituting magnetic core, their equivalent outer sphere diameter, and the volume fraction of magnetic materials contained in it. The three parameters must be as large as possible, which is favored by compact structures (having a high volume magnetization) rather than loose aggregates (having a small magnetic volume fraction). Increasing these three parameters will increase the r_2 relaxivity up to a maximum, corresponding to the MAR–SDR transition. Besides, the hydrodynamic diameter of MRI contrast agents must not exceed an upper limit classically estimated around 300 nm to enable sufficiently long half-life inside the blood vessels (Okuhata, 1999), when intravenously administrated, otherwise, they are rapidly cleared by the reticuloendothelial system.

Starting from iron oxide spinel system, and particularly the most used maghemite one, the magnetization increase can be achieved by replacing it by cobalt ferrite. The magnetization of bulk $CoFe_2O_4$ is about 85–90 emu g^{-1} while that of bulk γ-Fe_2O_3 does not

exceed 75 emu g^{-1} (Valenzuela, 1995). $CoFe_2O_4$ nanoferrites have been widely considered for various nanomedicine applications (Davies et al., 1995; Veverka et al., 2007; Joshi et al., 2009; Bregar et al., 2013; Salunkhe et al., 2013), and the replacement of maghemite by cobalt ferrite may be considered for biological applications if the absence of cobalt cation release, suspected to induce oxidative stress and cell toxicity, is demonstrated. Then, the substitution, in these ferrites, of a controlled amount of Co^{2+} by diamagnetic Zn^{2+} and Fe^{3+} by paramagnetic high spin lanthanide Ln^{3+} would significantly increase the total magnetization (Kolekar et al., 1994; Tahar et al., 2008; Pilati et al., 2018). The rationale is that, according to the collinear ferrimagnetic Néel model, a decrease of the magnetic moment of the tetrahedral spinel sub-lattice and an increase of the magnetic moment of the octahedral spinel sub-lattice both lead to an increase of the total magnetic moment of the spinel crystal. It may be noticed that, because of their ionic respective radii, lanthanide ions prefer the octahedral spinel sites (Kolekar et al., 1994; Yan et al., 1999; Tahar et al., 2008; Pilati et al., 2018), while zinc ions prefer the tetrahedral sites (Petitt and Forester, 1971; Ammar et al., 2006).

To date, wet chemistry has allowed the production of such mixed Co ferrite NPs, yet only substituted by either Zn or Gd, but not simultaneously. A rapid overview of the relevant literature shows that chemically made $(Co_{1-x}Zn_x)Fe_2O_4$ nanocrystalline solid solutions exhibit a maximal magnetization at x ranging between 0.4 and 0.5 (Sharifi and Shokrollahi, 2012; Tahar et al., 2012; Ghasemian et al., 2015; Tatarchuk et al., 2017). In the case of $Co(Fe_{1-x}Ln_x)O_4$ nanocrystalline solid solutions, the highest magnetization was obtained for Ln = Gd and $x \sim 0.1$, the solubility limit of Ln cations being of the same order (Tahar et al., 2007; Kumar et al., 2011).

These substitutions may affect the Curie temperature T_C of the spinel phase. T_C is indeed closely related to the number of linkages between 3d transition paramagnetic ion cations through oxygen anions per formula unit (Gilleo, 1960). This number decreases when diamagnetic or weakly interacting 4f cations are introduced into the spinel lattice, reducing the T_C value. This feature must be controlled because a T_C decrease lowered down to the body temperature makes the produced particles paramagnetic and less valuable for negative MRI (Mertz et al., 2017; Shlapa et al., 2016).

In this context, we prepared a series of nanometer-sized $Co_{0.6}Zn_{0.4}Fe_{2-x}Gd_xO_4$ NPs, varying the Gd^{3+} concentration up to its solubility limit and characterizing their structural and magnetic properties. We then evaluated their colloidal stability in water when they were coated by a hydrophilic ligand, typically positively charged dopamine (DA) species, and we measured their longitudinal and transversal relaxivities in water at an applied static field of 1.41 T that is close to the value of 1.5 T used in most clinical magnetic resonance imagers. Finally, we evaluated their cytotoxicity on model healthy human cells, with a special emphasis on their capability to be used as efficient magnetic probes for biomedical imaging.

Results and Discussion

Gd^{3+} solubility limit

The X-ray diffraction (XRD) patterns of all the prepared Gd-substituted particles were recorded. All were indexed within the cubic spinel structure without evidence of any trace of impurities (Fig. SI-1). In addition, all the diffraction lines are broadened in agreement with the formation of ultrafine crystals. A close look at the most intense (311) diffraction peak revealed a slight shift toward lower diffraction angles, particularly for the lowest nominal Gd compositions (Fig. 1), indicating a progressive increase of the unit spinel cell constant. This increase is compatible with cationic radii change by substituting the Fe^{3+} ions by larger Gd^{3+} (0.940 vs. 0.645 Å; Shannon, 1976). The Rietveld refined unit cell parameters were found to be slightly higher than that reported for similarly prepared $Co_{0.6}Zn_{0.4}Fe_2O_4$ particles. Noteworthy, the variation of the unit cell parameters as a function of the nominal Gd composition, x_{nom}, was not trivial. In particular, no Vegard law was evidenced.

The chemical composition of all the prepared ferrites was accurately determined by X-ray fluorescence (XRF) spectroscopy analysis (selected spectra are given in Fig. SI-2). All the metallic Co, Zn, Fe, and Gd elements were detected, and their measured atomic contents allowed us to formulate each produced spinel phase (Table 1), evidencing an increasing elemental chemical composition departure from the nominal composition.

The most noticeable change relatively to the nominal composition is revealed for Gd, indicating the existence of a solubility limit of this element in the host spinel lattice. In order to gain further information about the solubility limit upon Fe^{3+} substitution by Gd^{3+}, we

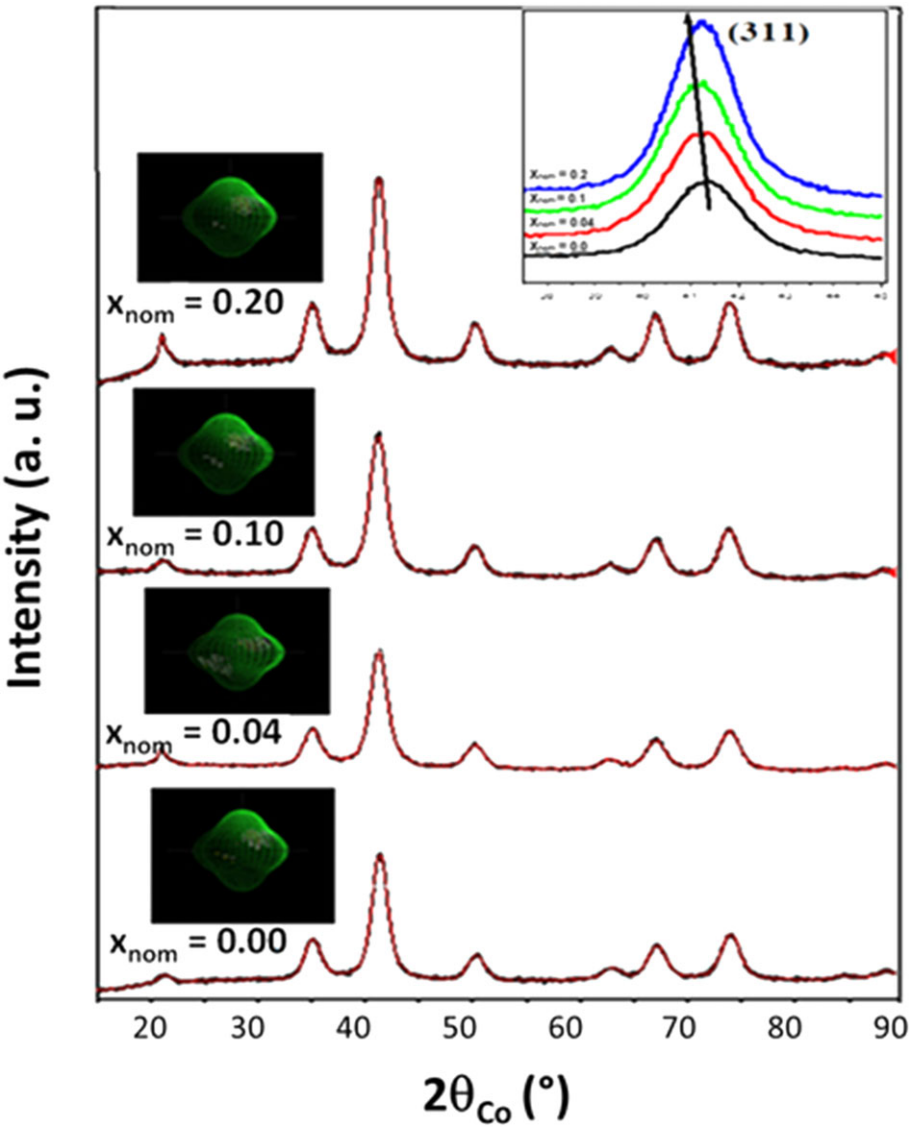

Figure 1. X-ray diffraction patterns of the $Co_{0.6}Zn_{0.4}Fe_{2-x}Gd_xO_4$ particles produced with a nominal Gd composition x_{nom} = 0, 0.04, 0.10 and 0.20. The continuous red line corresponds to the MAUD's fits. The crystallite shape inferred from MAUD analysis is given for each sample.

plotted the experimental atomic ratio of gadolinium to total gadolinium and iron elements, $[Gd]_{exp}/[Fe + Gd]_{exp}$, versus its associated nominal content, x_{nom} (Fig.SI-3). The experimental ratio initially increased monotonically with increasing nominal ratio and then reached a plateau at about 3% for a nominal value of Gd of x_{nom} = 0.10 associated to the sample having the experimental chemical composition of $Co_{0.56}Zn_{0.33}Fe_{2.03}Gd_{0.06}O_4$.

This solubility limit of 0.06 is in the same range than values reported in the literature on differently prepared lanthanide substituted spinel ferrites. Rezlescu et al. (1997) and Ahmed et al. (2005) evidenced a limit value of $x_s < 0.01$ and $x_s < 0.05$ in solid state made $Ni_{0.7}Zn_{0.3}Fe_{1-x}Ln_xO_4$ (Ln = Yb, Er, Dy, Tb, Gd, Sm, and Ce) and $Ni_{1-y}Zn_yFe_{2-x}Ln_xO_4$ (Ln = La) particles, respectively. Kolekar et al. (1994), Tahar et al. (2008), and Kahn and Zhang (2001) determined a limit value of x_s = 0.10 and x_s = 0.06, respectively, in wet-chemically made $CoFe_{2-x}Ln_xO_4$ (Ln = Gd, Sm, Eu, Nd, Ho) and $CoFe_{2-x}Ln_xO_4$ (Ln = Ce, Ln = Ce, Sm, Eu, Gd, Dy, Er) particles, respectively. The low Gd solubility limit is mainly attributed to the high ionic radius of Gd^{3+}. It is a reasonable approximation indeed that a $(Co_{1-x}Zn_x)(Fe_{2-y}Gd_y)O_4$ solid solution crystallizes in the inverse spinel structure, in which almost all the Co^{2+} and Zn^{2+} cations are respectively octahedrally and tetrahedrally coordinated. As a

Table 1. The unit cell parameter and the XRF chemical analysis of all the produced nanoferrites.

x_{nom}	a (Å) ±0.005	XRF chemical composition ±0.02
0.00	8.423	$Co_{0.60}Zn_{0.40}Fe_{2.00}O_4$
0.02	8.426	$Co_{0.60}Zn_{0.40}Fe_{1.99}Gd_{0.01}O_4$
0.04	8.428	$Co_{0.60}Zn_{0.40}Fe_{1.98}Gd_{0.02}O_4$
0.06	8.429	$Co_{0.60}Zn_{0.40}Fe_{1.97}Gd_{0.03}O_4$
0.08	8.429	$Co_{0.60}Zn_{0.40}Fe_{1.96}Gd_{0.04}O_4$
0.10	8.430	$Co_{0.60}Zn_{0.40}Fe_{1.94}Gd_{0.06}O_4$
0.12	8.431	$Co_{0.60}Zn_{0.40}Fe_{1.94}Gd_{0.06}O_4$
0.18	8.429	$Co_{0.62}Zn_{0.38}Fe_{1.94}Gd_{0.06}O_4$
0.20	8.422	$Co_{0.59}Zn_{0.41}Fe_{1.94}Gd_{0.06}O_4$

XRF, X-ray fluorescence.

consequence, the inter-ionic cation-oxygen distances $R_{B\text{-}O}$, defined as the average cation-oxygen bond length on octahedral spinel sites, can be expressed as (Salah, 2006; Beji et al., 2015):

$$R_{B-O} = y \cdot {r_{Gd}}^{3+} + (1-x) \cdot {r_{Co}}^{2+} + (1+x-y) \cdot {r_{Fe}}^{3+} + {r_O}^{2-}. \quad (2)$$

Using the values of ionic radii determined by Shannon (1976) and refined by O'Neil and Navrotsky (1984) (Table SI-1), a site size contraction of about 0.005 Å can be observed between the calculated $R_{B\text{-}O}$ values in $CoFe_2O_4$ and $Co_{0.6}Zn_{0.4}Fe_2O_4$. This size contraction in octahedral sites seems to be sufficient to notably reduce the solubility limit of Gd^{3+} from x_s = 0.10 to x_s = 0.06 in $Co_{0.6}Zn_{0.4}Fe_{2-y}Gd_yO_4$ mixed ferrite NPs by comparison with $CoFe_{2-y}Gd_yO_4$ ones (Kolekar et al., 1994; Tahar et al., 2008). Even a small decrease in $R_{B\text{-}O}$ can lead to much more energy required for Gd^{3+} to enlarge the B sites and enter in them.

To try establishing experimentally this feature, the infrared spectra of representative samples (mainly those corresponding to a nominal Gd composition smaller or equal to 0.1) were recorded (Fig. 2). Focusing on the spinel oxide skeleton vibrations, four infrared active modes, called ν_1, ν_2, ν_3, and ν_4, are expected at 650–550, 530–390, 380–340, and 300–200 cm^{-1}, respectively (Waldron, 1955; White and DeAngelis, 1967). The former bands (ν_1 and ν_2) are ascribed to the intrinsic vibrations of tetrahedral and octahedral metal-oxygen complexes, while the latter (ν_3 and ν_4) are related to more complex vibrations. Besides, their energy positions and intensities are strongly dependent on the nature and oxidation state of the metal cations. Therefore, valuable information can be obtained on the local structure of the studied phases by the analysis of their infrared spectra in these wavelength ranges (Waldron, 1955; Nasrazadani and Raman, 1993; Salah, 2006). Careful observation of the recorded spectra allowed us to distinguish two main regions: beyond ~800 cm^{-1} and below ~700 cm^{-1}. In the first region, the spectra show bands characteristic of chemisorbed species including water, polyol, and acetate ions (see Supporting Information) (Ammar et al., 2001). In the second region, they show the spinel lattice vibration bands (Table 2).

Focusing on the ν_2 band, its energy position varies when the composition of the investigated ferrites changes (see the dotted line in the right part of Fig. 2). This variation traduces changes in the metal-oxygen distances in the octahedral spinel sites and in the metal atomic masses. A decrease of the wavenumber means a decrease of the bonding length, and an increase of the metal atomic mass: ν_2 value is found to be 409 cm^{-1} in $Co_{0.60}Zn_{0.40}Fe_{2.00}O_4$ particles and

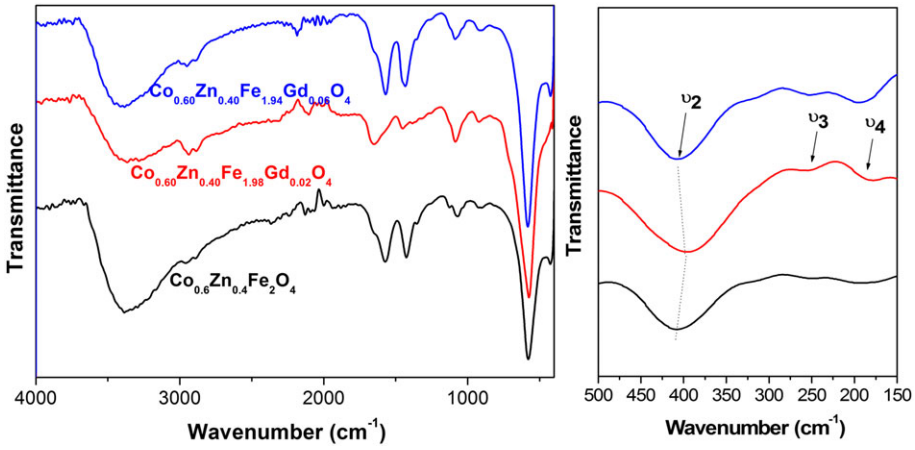

Figure 2. Medium (left) and far (right) infrared spectra of representative samples.

Table 2. Assignment of infrared and Raman main bands of representative samples.

	FIR			
	υ_1 (cm^{-1}) ±4	υ_2 (cm^{-1}) ±4	υ_3 (cm^{-1}) ±4	υ_4 (cm^{-1}) ±4
$Co_{0.6}Zn_{0.4}Fe_{2.00}O_4$	582	409	249	186
$Co_{0.6}Zn_{0.4}Fe_{1.98}Gd_{0.02}O_4$	576	396	255	182
$Co_{0.6}Zn_{0.4}F0e_{1.94}Gd_{0.06}O_4$	579	400	248	192
	Raman			
	$\upsilon(E_g)$ (cm^{-1}) ±2	$\upsilon(T_{2g})$ (cm^{-1}) ±2	$1^{st}\upsilon(A_{1g})$ (cm^{-1}) ±2	$2^{sd}\upsilon(A_{1g})$ (cm^{-1}) ±2
$Co_{0.6}Zn_{0.4}Fe_{2.00}O_4$	291	470	659	
$Co_{0.6}Zn_{0.4}Fe_{1.98}Gd_{0.02}O_4$	316	475	674	
$Co_{0.6}Zn_{0.4}Fe_{1.94}Gd_{0.06}O_4$	319	465	669	

FIR, far-infrared.

decreases down to 393 cm^{-1} in those corresponding to the $Co_{0.60}Zn_{0.40}Fe_{1.98}Gd_{0.02}O_4$ final composition, in agreement with the insertion of a nonzero amount of large and heavy Gd^{3+} ions in the octahedral lattice sites. Surprisingly, by increasing the nominal Gd content, ν_2 increased up to 400 cm^{-1}, as ascribed to subsequent decrease of the average metal-oxygen distance, which can in turn be explained by the departure of a certain quantity of Co^{2+} ions from B to A sites (with the transfer in the opposite direction of the same number of Fe^{3+} ions of lower ionic radius) to induce a certain relaxation of the spinel lattice upon insertion of increasing quantities of Gd^{3+}. In other words, whereas $Co_{0.60}Zn_{0.40}Fe_{2.00}0_4$ particles exhibit a spinel structure close to the thermodynamically stable one, in which almost all the Co^{2+} and Zn^{2+} cations are octahedrally and tetrahedrally coordinated, respectively, Gd^{3+}-substituted particles depart from this structure with a nonzero amount of tetrahedrally Co^{2+} coordinated cations.

To complete these investigations, Raman spectroscopy was performed on the same samples and on bulk $CoFe_2O_4$, which serves as reference. All the recorded spectra were characteristic of the cubic spinel structure (Fig. 3). Usually five active modes, one of E_g symmetry, two of T_{2g}, and two of A_{1g} are observed. The modes, which mainly involve the motion of oxygen in both tetrahedral and octahedral sites, appeared in the low frequency range ~200–750 cm^{-1} (White and DeAngelis, 1967; Nasrazadani and Raman, 1993; Kreisel

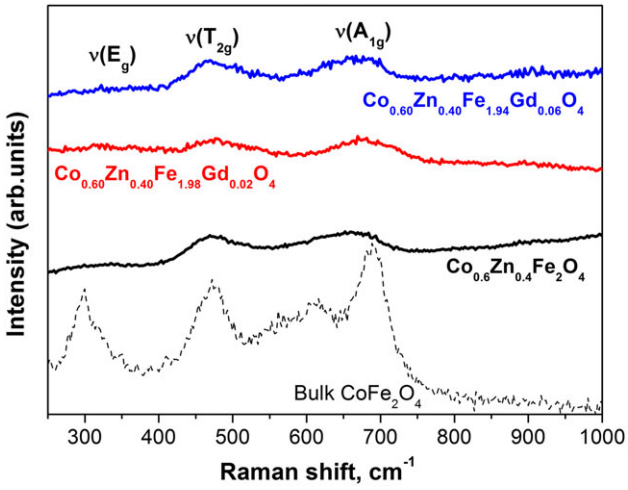

Figure 3. Raman spectra of representative samples compared with that of bulk $CoFe_2O_4$.

et al., 1998; Wang et al., 2003). Among these modes, those which mostly correspond to the motion of oxygen in metal-oxygen tetrahedral complexes appear above 600 cm^{-1}, while those mainly reflecting the stretching vibrations of metal-oxygen octahedral complexes appear at higher frequencies, as summarized in Table 2. At first sight, the Raman spectra of our particles exhibit clearly broadened bands compared with bulk $CoFe_2O_4$. This feature is quite common in nanostructures (Yu et al., 2002; Tahar et al., 2007; Kumar et al., 2011). Moreover, the bands above 600 cm^{-1}, related to the two A_{1g} modes, are found to overlap, in accordance with previous works on nanocrystalline spinel ferrites (da Silva et al., 2010; Kumar et al., 2016). Finally, the band at around 200 cm^{-1} (not shown), usually related to one of the T_{2g} modes, is very weak in intensity and hard to detect at ambient temperature (Shebanova and Lazor, 2003; Kumar et al., 2016). Now, comparing the band energy position of our samples (Table 2) with those of bulk $CoFe_2O_4$ (a pure inverse spinel) on the one hand, and with those of each other on the other hand, relative shifts were observed with Gd content increase. These shifts are ascribed to the changes in the metal-oxygen bond lengths within both the tetrahedral and octahedral spinel sub-lattices with the introduction of large Gd^{3+} cations. In other words, Gd^{3+} incorporation affects the average length of the metal-oxygen bonds in both octahedral and tetrahedral complexes. As suggested by infrared spectroscopy, Raman spectroscopy confirmed the cation migration between the spinel sub-lattices. Although they are weak, these structural changes explain why we did not observe a Vegard law for the variation of the unit cell parameter of the studied solid solution as a function of its Gd composition. They also suggest nontrivial variations of their magnetic properties with their composition, particularly their magnetocrystalline anisotropy and their total magnetization. Whereas a simple increase of the magnetization was expected by replacing Fe^{3+} cations by Gd^{3+}, namely, by replacing cations leaving a magnetic moment of 5 μ_B by ones leaving a magnetic moment of 7 μ_B, the displacement of Co^{2+} cations from the octahedral to the tetrahedral sites and reversely, the displacement of an equal amount of Fe^{3+} cations from the tetrahedral to the octahedral sites should decrease the total magnetocrystalline anisotropy constant (lower spin-orbit coupling in the B sub-lattice) and increase the total crystal magnetization (smaller magnetic moment in the A sub-lattice).

Microstructural properties

From the acquired XRD data, the average crystal size, $<L_{XRD}>$, and the micro-deformation, $<\varepsilon>$, were determined for all the produced nanoferrites. They were found to be consistent with 6 nm sized almost isotropic in shape strain free crystals. The incorporation of Gd^{3+} within its solubility limit did not induce apparent distortions in the spinel lattice: $<\varepsilon>$ ranged between 1.5% and 2.0%. These results were confronted to those obtained by transmission electron microscopy. Representative micrographs showed roughly spherical particles, slightly agglomerated, with an average size ranging between 5 and 6 nm (Fig. 4), suggesting that the produced NPs are consistent with single crystals, interacting mutually magnetically. They appeared as almost uniform in size, and the statistical analysis of hundreds of particles considered as spheres agreed with a standard size deviation of less than 15%. Such low size dispersity can be underlined because it suggests a rather uniform magnetic response of these NPs under magnetic stimuli.

High-resolution transmission electron microscopy observations confirmed that all the produced NPs

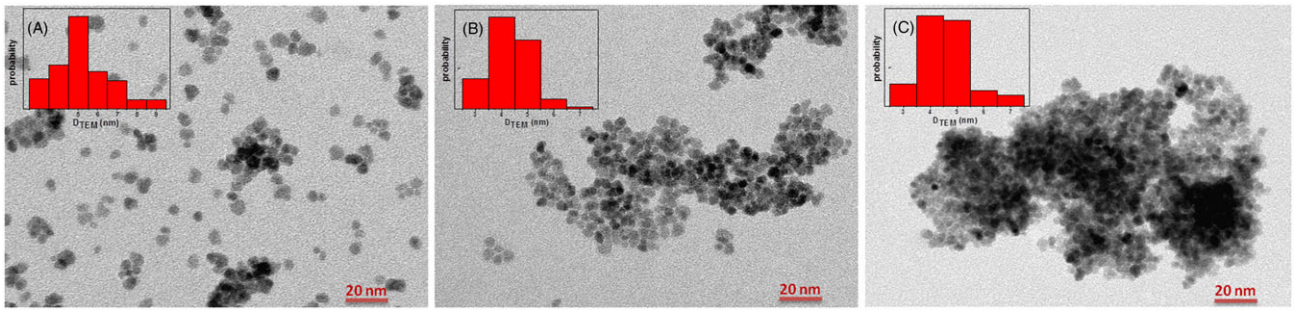

Figure 4. Transmission electron microscopy (TEM) images and related size distribution (in the inset) of (A) $Co_{0.6}Zn_{0.4}Fe_2O_4$, (B) $Co_{0.6}Zn_{0.4}Fe_{1.98}Gd_{0.02}O_4$, and (C) $Co_{0.6}Zn_{0.4}Fe_{1.94}Gd_{0.06}O_4$ particles.

were single crystals. All images show fringes corresponding to crystallographic planes of the cubic spinel lattice. There was no evidence of structural defects such as dislocations, stacking faults, nor surface amorphous region, establishing their high crystalline quality despite their reduced size and their local structural changes induced by Gd incorporation. A zoomed picture of one representative particle among the studied nanocrystalline $Co_{0.6}Zn_{0.4}Fe_{2-x}Gd_xO_4$ ($0 \leq x \leq 0.06$) solid solutions is shown in Figure 5. From all these observations, one may expect relevant magnetic properties for the desired application, because a high crystalline quality usually means less broken magnetic pathways and then higher specific magnetization.

Magnetic properties

Direct current (DC) magnetic measurements were performed on three selected samples: $Co_{0.60}Zn_{0.40}Fe_{2.00}0_4$, $Co_{0.60}Zn_{0.40}Fe_{1.98}Gd_{0.02}O_4$, and $Co_{0.60}Zn_{0.40}Fe_{1.94}Gd_{0.06}O_4$, corresponding to nominal Gd compositions of $x_{nom} = 0.0$, 0.04, and 0.10, respectively, and assumed to be representative of the general magnetic features of the produced nanocrystalline solid solutions. In practice, the zero field cooling (*ZFC*) and field cooling (*FC*) thermal variation of the *DC* magnetic susceptibility, $\chi(T)$, were recorded on the samples on their powder form and depicted in Figure 6. A net irreversibility was thus evidenced between the *ZFC*- and *FC*-$\chi(T)$ branches in agreement with a superparamagnetic behavior. *ZFC*-$\chi(T)$ exhibits a narrow peak at a critical temperature defined as the average blocking temperature T_B, while the *FC*-$\chi(T)$ curve reaches a plateau below T_B. T_B represents the threshold temperature above which the magnetic anisotropy barrier is overcome by thermal activation energy alone, causing the transition of the magnetic NPs from their ferrimagnetic state to the relaxed superparamagnetic one and reversely. The T_B value is directly related to the volume of the magnetic particles. It increases when the size increases, and it becomes widely distributed when the distribution of the size is broadened. For a given average size, T_B also increases with the effective magnetic anisotropy constant, K_{eff}. Finally, T_B is also affected by the strength of dipolar interactions. It is shifted toward higher temperatures when these interactions between magnetic moments are stronger. Therefore, comparing now the T_B values measured on our samples, supposed to consist in strongly and similarly interacting almost uniformly and similarly sized magnetic single nanocrystals, we found that they increased slightly from about 150 K in Gd-free NPs to about 165 K in the Gd-richest NPs (Table 3).

Meanwhile, the magnetic susceptibility values at the *ZFC*-$\chi(T)$ maximum increased too. This T_B shift toward higher temperature can be theoretically explained by three raisons: (1) an average particle

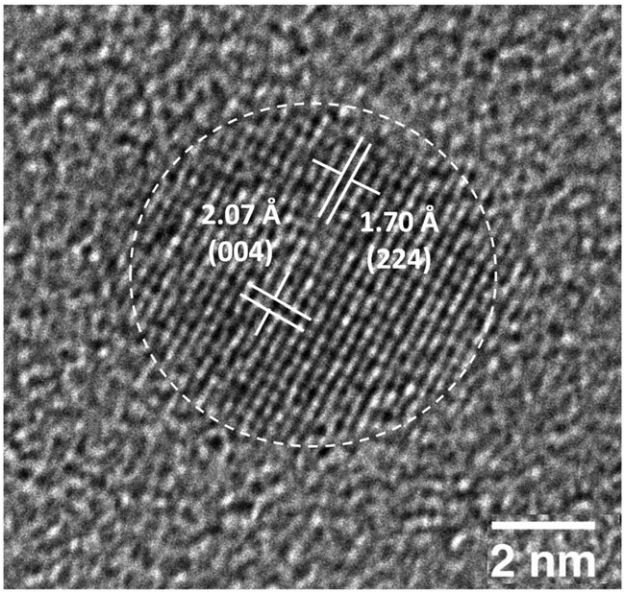

Figure 5. High-resolution transmission electron microscopy view of a representative particle ($x = 0$) of the produced nanocrystalline $Co_{0.6}Zn_{0.4}Fe_{2-x}Gd_xO_4$ solid solution, with the indication of some reticular distances matching well with the $Co_{0.6}Zn_{0.4}Fe_2O_4$ spinel structure (ICDD no. 98-016-6202).

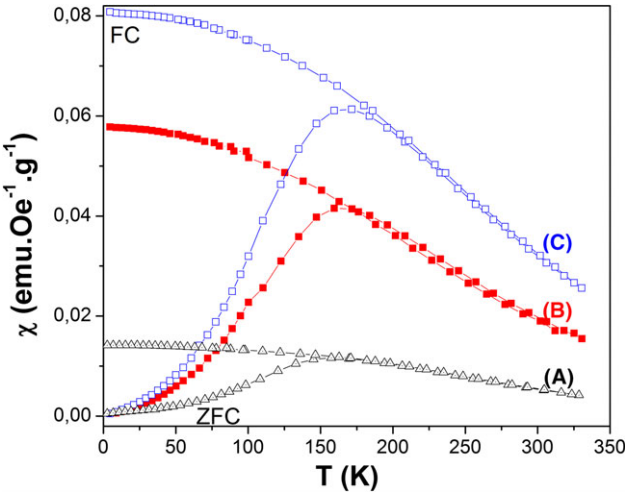

Figure 6. Field cooling (FC) and zero field cooling (ZFC) thermal variation of the dc-magnetic susceptibility measured at a magnetic field of 200 Oe on the as-produced (A) $Co_{0.6}Zn_{0.4}Fe_2O_4$, (B) Co0.60Zn0.40$Fe_{1.98}Gd_{0.02}O_4$, and (C) Co0.6$Zn_{0.4}Fe_{1.94}Gd_{0.06}O_4$ nanoparticles.

Table 3. Main magnetic properties of representative polyol-made $Co_{0.6}Zn_{0.4}Fe_{2-x}Gd_xO_4$ nanoparticles.

x	T_B (200 Oe) K ±2	M_{sat} (300 K) emu g^{-1} ±1	M_{sat} (5 K) emu g^{-1} ±1	H_c (5 K) kOe ±50	T_C K ±10
0.00	151	77	118	4040	612
0.02	155	78	129	4350	555
0.06	168	80	133	4490	554

size increase from one sample to another, (2) an increase of anisotropy constant K_{eff} when x increases in the $Co_{0.60}Zn_{0.40}Fe_{2-x}Gd_xO_4$ nanocrystalline solid solution, and/or (3) an increase of dipolar interaction strength when x increases due to an increase of the total magnetic moment with x. Because the size of all the produced particles is supposed to be constant, and the magnetocrystalline anisotropy is expected to be quite unchanged by introducing Gd in the spinel lattice, only dipolar interactions would be incriminated. Dipolar interactions refer to the direct interaction between two magnetic domains bearing a given magnetic moment and separated by a given distance. The dipole interaction energy is proportional to the square of the magnetic moments and inversely proportional to the cube of the distance (Mørup et al., 2010). This distance is assumed to be constant in all the samples, while the average magnetic moment is expected to increase from one sample to another by increasing the Gd content.

Pursuing our magnetic investigations, we decided to perform further magnetic measurements on weakly interacting particles, to avoid any dipolar interaction interferences. In practice, the produced particles were mixed, by soft milling, with a diamagnetic alumina matrix (4.2 wt.%), and their first magnetization curves (Fig. 7) as well as their hysteresis loops (Fig. 8) were recorded at different temperatures. The collected magnetic data were then corrected from the diamagnetic alumina contribution and expressed per gram of magnetic $Co_{0.6}Zn_{0.4}Fe_{2-x}Gd_xO_4$ NPs.

As expected, $M(H)$ curves did not evidence any hysteresis feature when cycling the applied magnetic field between 50 and −50 kOe at 300 K (data not shown). On the contrary below T_B, typically at 5 K, they did show a hysteresis, with a coercivity of around 4 kOe and a remanence of more than 50% (Fig. 8).

Using these data, the saturation magnetization, M_{sat}, was determined by extrapolating M versus $1/H$ curve to $1/H = 0$. The inferred values were found to be relatively

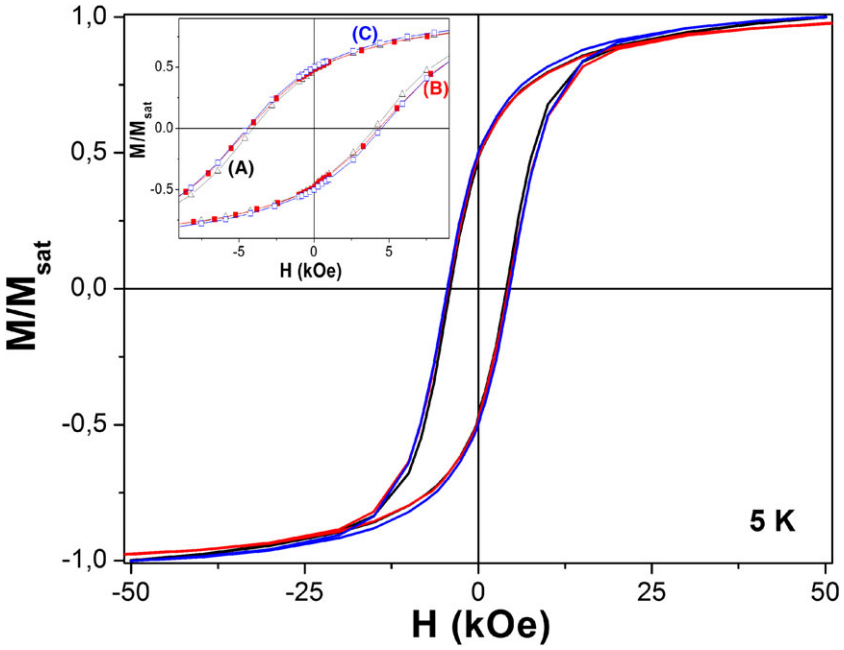

Figure 7. Variation of the normalized zero field cooling magnetization as a function of the magnetic field measured at 5 K on (A) $Co_{0.6}Zn_{0.4}Fe_2O_4$, (B) $Co_{0.6}Zn_{0.4}Fe_{1.98}Gd_{0.02}O_4$, and (C) $Co_{0.6}Zn_{0.4}Fe_{1.94}Gd_{0.06}O_4$ nanoparticles dispersed in an alumina matrix.

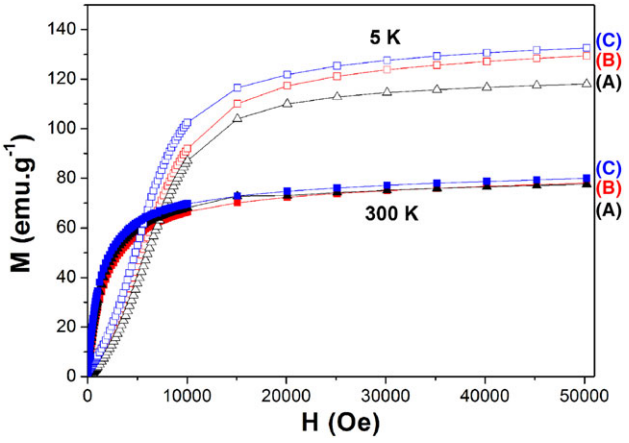

Figure 8. First magnetization curves recorded at 300 and 5 K on (A) $Co_{0.6}Zn_{0.4}Fe_2O_4$, (B) $Co_{0.6}Zn_{0.4}Fe_{1.98}Gd_{0.02}O_4$, and (C) $Co_{0.6}Zn_{0.4}Fe_{1.94}Gd_{0.06}O_4$ nanoparticles dispersed in an alumina matrix.

high, close to 80 and 130 emu g^{-1} at 300 and 5 K, respectively, for all the Gd-substituted samples, increasing slightly by increasing the Gd content (Table 3).

The temperature dependence of the spontaneous magnetization, M_{sp}, measured at high field, typically 50 kOe, was also plotted to be tentatively used to estimate the Curie temperature of the produced particles (Fig. 9). Within the Bloch (1930) model, the thermal variation of M_{sp}, in a temperature range far below T_C, can be used to estimate T_C (Hendriksen et al., 1993; Chen et al., 1996; Ngo et al., 2001; Demortière et al., 2011; Basti et al., 2014) according the following equation:

$$M_{sp}(T) = M_{sp}(0)\left[1 - (T/T_C)^{\beta}\right], \quad (3)$$

where β is the so-called Bloch's exponent and $M_{sp}(0)$ is the spontaneous magnetization at 0 K. β is usually set at 1.5 for bulk ferromagnets and ferrimagnets (Bloch, 1930). It is also equal (Ammar et al., 2006; Basti et al., 2014; Hanini et al., 2016) or slightly smaller (Hendriksen et al., 1993; Chen et al., 1996;

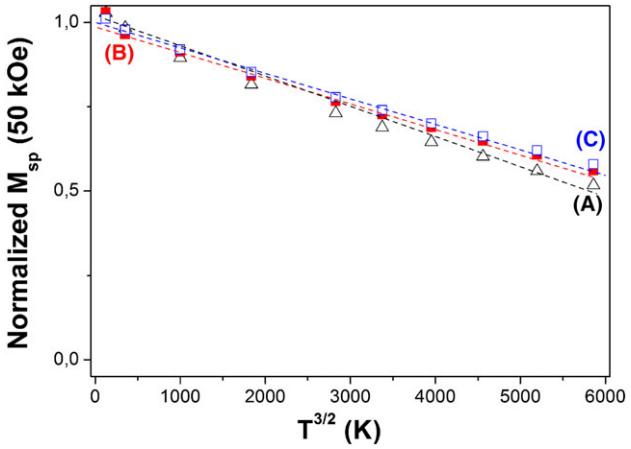

Figure 9. Thermal variation of the normalized spontaneous magnetization measured at 50 kOe and defined as $M_{sp}(T)/M_{sp}(0)$, for (A) $Co_{0.6}Zn_{0.4}Fe_2O_4$, (B) $Co_{0.6}Zn_{0.4}Fe_{1.98}Gd_{0.02}O_4$, and (C) $Co_{0.6}Zn_{0.4}Fe_{1.94}Gd_{0.06}O_4$ nanoparticles. The discontinuous lines correspond to the best linear fits.

Zhang et al., 1998; Ngo et al., 2001; Demortière et al., 2011) than 1.5 for nanocrystals, depending on their size and their crystallinity. In the present case, based on the high-resolution transmission electron microscopy results, β was set at 1.5, and the experimental data were fitted to estimate T_C. Values ranging between 543 and 566 K were obtained (Table 3), without evidencing a clear dependence on the Gd content. These values are far from the body temperature, making the engineered nanoferrites valuable negative contrast agents for MRI.

Colloidal stability and magnetic resonance imaging relaxivity

To evaluate the MRI contrasting ability of the produced NPs, it is important to disperse them in an aqueous medium as stable colloids. A catechol ligand bearing an amino group, also known as dopamine (DA), was grafted onto the surface of the particles to make them repulsive and slightly positively charged in physiological pH conditions (Figure 10). A specific protocol was developed, adapted from an already established one (Basti et al., 2010; Fouineau et al., 2013) to attach the required amount of DA at the surface of the NPs, favoring weak yet nonzero clustering. The idea was to form small controlled aggregates of less than 100 nm in hydrodynamic diameter to improve the total relaxivity of the particles without furtherly limiting their circulation time inside the blood vessels, when administrated intravenously.

At first, the grafting yield was checked by both X-ray photoelectron spectroscopy (XPS) and thermogravimetric analysis (TGA). In particular, the replacement of the residual polyol (and/or acetate) molecules adsorbed at the surface of the as-produced particles by DA ligands was confirmed, mainly by the appearance of nitrogen XPS signature only in the functionalized NPs (Fig. SI-4). Moreover, the weight content of DA was quantified by TGA as 45 wt.% in the studied hybrids (Fig. SI-5).

Secondly, the zeta potential was measured on the aqueous suspensions of bare and DA grafted NPs, by varying the pH from 2 to 12 (Fig. SI-6). Positive charges were evidenced up to isoelectric points at pH = 7 and 9 (close to the tabulated pKa value of 8.93 for DA) on bare and functionalized NPs, respectively. These surface charges render the functionalized particles hydrophilic at physiological pH and should avoid their flocculation in water, when also combined with the steric repulsions due to the organic shell.

Thirdly, dynamic light scattering (DLS) measurements were carried out on the two suspensions at neutral pH. While a hydrodynamic diameter of several hundreds of nanometer was measured for bare particles, indicating their large aggregation, a value close to 50 nm (monomodal size distribution) was measured for the functionalized particles, suggesting their limited clustering (Fig. 11). In particular, the effect of a pulsed ultrasound treatment (repeated cycles 2″ on at full power, 1″ off, during 10′) was tested to tentatively decrease the hydrodynamic size by breaking the clusters, yet it did not succeed. This moderate clustering, because of the balance between electro-steric repulsions between the weakly positively charged DA-grafted particles and their mutual magnetic and van der Waals attractions, was

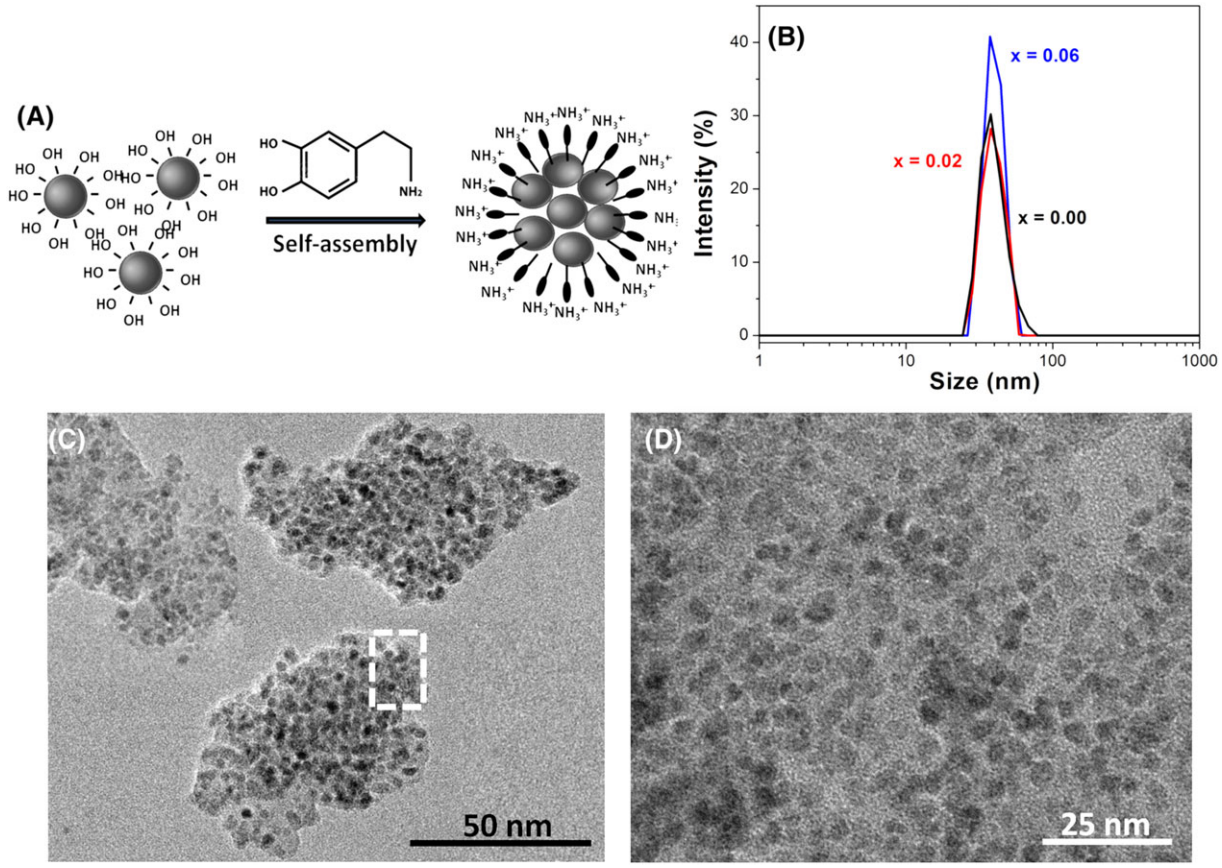

Figure 10. (A) Schematic presentation of the clustering of the $Co_{0.6}Zn_{0.4}Fe_{2-x}Gd_xO_4$ nanoparticles decorated by positively charged dopamine ligands. The attachment of dopamine is achieved by diol complexation of surface Fe^{3+} cations. (B) Hydrodynamic size distribution of the related nanohybrids when dispersed in deionized water. (C) Representative transmission electron microscopy micrograph of the formed clusters and (D) a zoom on a selected area of a cluster highlighting the nonzero distance between adjacent particles ascribed to the organic coating.

also confirmed by transmission electron microscopy observations (Fig. 11) of drops from the resulting suspensions deposited on the carbon grids.

As for the proton relaxation properties, the prepared aqueous colloidal suspensions diluted to total metal concentrations ranging from ~0.05 to ~0.8 mM depending on the samples were supposed to verify the Redfield condition defining the MAR model (Vuong et al., 2012). In other words, freely diffusing water molecules, surrounding the previously described magnetic clusters, explore a space larger than the NP volume during one echo time of the applied radiofrequency sequence. The theoretical estimation of the transversal relaxivity of the studied systems becomes possible even if their composition is far from that of maghemite or magnetite. Replacing maghemite or magnetite spinel phase by a Zn-substituted and Gd-substituted cobalt ferrite should not affect significantly the value of the molar volume v_{mat} in equation 1a. A variation of only ±5% is expected on the $1.5{\cdot}10^{-5}$ m^3 mol^{-1} maghemite v_{mat} value (Vuong et al., 2012). Using equation 1 with the experimental values of M_v and approximating d by the experimental $<D_{DLS}>$, an r_2 value of less than 10 mM^{-1} sec^{-1} was estimated theoretically on the studied sample series, far below our expectations.

However, when we directly performed relaxivity measurements to assess the exact efficiency of our prepared batches to relax nuclear spins of water protons, we found much higher relaxivity values. In practice, their transverse (r_2) and longitudinal (r_1) relaxivities were measured at physiological temperature, 37°C, with a 60-MHz relaxometer (Bruker Minispec™ mq60) based on a 1.41-T magnet (i.e., close to the 1.5-T magnetic field of most clinical MRI machines used in hospitals). More precisely, the longitudinal (T_1) and transverse (T_2) relaxation times of water protons were measured with respectively an inversion-recovery and a Carr-Purcell-Meiboom-Gill (CPMG) sequence, at decreasing equivalent [Fe] concentrations from 0.8 to 0.1 mM. The receiver gain

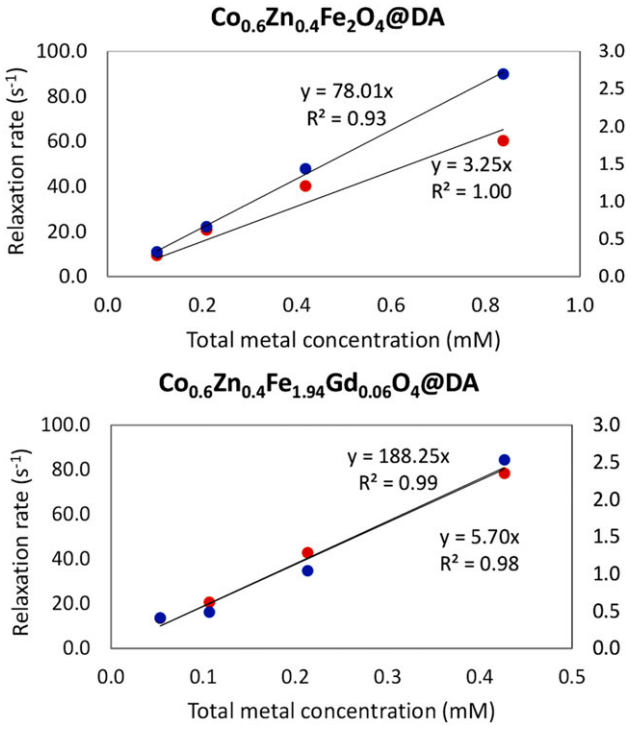

Figure 11. Relaxation rates $R_2^{NP} - R_2^{water} = 1/T_2 - 1/T_2^{water}$ (red data points) and $R_1^{NP} - R_1^{water} = 1/T_1 - 1/T_1^{water}$ (blue data points) variation as a function of the total metal cation concentration measured on dopamine (DA)-coated $Co_{0.6}Zn_{0.4}Fe_{2-x}Gd_xO_4$ (x = 0.0 and 0.06) nanoparticles dispersed in deionized water (T_1^{water} = 3997 msec and T_2^{water} = 1020 msec) at 37°C for an applied static magnetic field of 1.41 T (60-MHz proton resonance frequency). The corresponding r_2 and r_1 relaxivities of the nanoparticles are deduced from the slopes of the curves.

was adjusted between 42 and 48 dB in order to obtain a proper signal-to-noise ratio without saturation. For the inversion-recovery sequence, initial delay time was adjusted around $T_1/10$, while the final delay was at least 3 T_1, and the recycling delay at least 5 T_1, according to recommendations for such measurements (Henoumont et al., 2009). Recycling delay was kept constant for the CPMG sequence, while choosing an echo time (TE) around $T_2/50$ and a number of data points of 150, the decay curve of transverse magnetization being fitted by a mono-exponential law.

Relaxivities were obtained, in deionized water, from the slope of the linear variation with the total metal concentration $[M]_{total}$ of the longitudinal (respectively transverse) decay rate of water proton spins after subtraction of respective value measured on pure water, according to

$$1/T_{i=1 \text{ or } 2} = r_{i=1 \text{ or } 2} \cdot [M]_{total} + (1/T_{i=1 \text{ or } 2})_{water}. \quad (4)$$

The obtained curves were plotted on Figures 11 and SI-7, and the measured relaxivity values were summarized in Table 4 and compared with those of some references (Table 5), namely, commercial iron oxide-based negative contrast agents (Ferridex, etc.) and to those of various highly magnetized nanometer-sized spinel ferrite particles, on the other hand. Clearly, the r_2 and r_2/r_1 values measured on our optimized system, DA coated and clustered $Co_{0.60}Zn_{0.40}Fe_{1.94}Gd_{0.06}O_4$ particles are very high, higher than those reported on previous systems, in almost the same operating MRI conditions. Typically, for the Gd-richest sample, an r_2/r_1 of 33 and an r_2 of 188 mM^{-1} sec^{-1} were obtained.

The discrepancy between the measured r_2 values and those calculated within the Vuong model suggests us that the very high magnetization of our particles makes them working in an intermediate regime, corresponding to the transition between the MAR and the SDR relaxation regimes.

Finally, the potential cytotoxicity of $Co_{0.6}Zn_{0.4}Gd_xFe_{2-x}O_4$ ($0.0 \leq x \leq 0.06$) NPs was investigated on human fibroblastic cells, which are common in cytotoxicity assays of magnetic NPs (Spirou et al., 2018). Typically, the cells were incubated for 24 h

Table 4. Determination of the longitudinal and transversal relaxivities of DA-coated $Co_{0.6}Zn_{0.4}Fe_{2-x}Gd_xO_4$ NPs dispersed in deionized water at 37°C for an applied static field of 1.41 T.

x	$[Fe]_{col.}$ mM	$[M]_{col.}$ mM	$[Fe]_{XRF}$ mM	$[M]_{XRF}$ mM	r_1 mM^{-1} sec^{-1}	r_2 mM^{-1} sec^{-1}	r_2/r_1	$<D_{DLS}>$ nm	PDI
0.00	14.8	16.2	14.1	15.5	3.2	78.0	24	57	0.22
0.06	11.1	13.9	4.74	5.92	5.7	188.3	33	48	0.18
$CoFe_2O_4$	18.5	25.6	8.05	11.1	2.3	100.3	44	52	0.10
γ-Fe_2O_3[†1]	19.0	19.0	14.0	14.0	2.7	72.7	27	57	0.22

The iron and total metallic ion concentration ([Fe] and [M] = [Fe] + [Co] + [Zn] + [Gd]) of the stock suspension, as inferred from X-ray fluorescence (XRF) and colorimetry (col.) analyses, were given. The obtained MRI data on or engineered probes were compared with those of similarly sized and prepared γ-Fe_2O_3 and $CoFe_2O_4$. DLS, dynamic light scattering; PDI, polydispersity index.

[1]The chemical composition of the polyol-made and water washed maghemite nanoparticles (dark red color) changed during dopamine (DA) grafting to become closer to that of magnetite (black color). Indeed, thanks to the Pi donor properties of DA, a non-negligible charge density is transferred from DA to the ferric surface cations, during the complexation reaction (Fouineau et al., 2013).

Table 5. Main magnetic resonance imaging characteristics of commercial negative contrast agent and those under investigation based on highly magnetized ferrite nanoparticles.

	Coating	$<L_{XRD}>$ nm	$<D_{DLS}>$ nm	B_0 T	r_2 mM^{-1} sec^{-1}	r_2/r_1
Feridex (Na et al., 2009)	Dextran	5	160	1.5	120	4
Resovist (Wáng and Idée, 2017)	Carboxydextrane	4	60	1.5	186	6
Sinerem (Na et al., 2009)	Dextran	6	45	1.5	65.0	-
$CoFe_2O_4$ (Na et al., 2009)	Dimercaptosuccinic acid	12	30	1.5	172	-
$NiFe_2O_4$ (Na et al., 2009)	Dimercaptosuccinic acid	12	30	1.5	152	-
$MnFe_2O_4$ (Na et al., 2009)	Dimercaptosuccinic acid	6	-	1.5	208	-
$MnFe_2O_4$ (Na et al., 2009)	Dimercaptosuccinic acid	9	-	1.5	265	-
$MnFe_2O_4$ (Na et al., 2009)	Dimercaptosuccinic acid	12	30	1.5	358	-
$Zn_{0.5}Co_{0.5}Fe_2O_4$ (Ghasemian et al., 2015)	Dimercaptosuccinic acid	16	40	1.5	28.8	50
$Zn_{0.5}Ni_{0.5}Fe_2O_4$ (Sattarahmady et al., 2016)	Dextran	20	-	1.5	82.1	-
$Zn_{0.4}Mn_{0.6}Fe_2O_4$ (Zahraei et al., 2015)	Chitosan	14	300	1.5	315.0[†1]	5[†1]
$Co_{0.6}Zn_{0.4}Fe_{1.94}Gd_{0.06}O_4$[†2]	Dopamine	6	65	1.41	188.3	33

r_2 values are expressed per millimolar of total metallic ions and were measured at 37°C. DLS, dynamic light scattering.

[1]Determined by millimolar of iron only.

[2]This work.

with different doses of DA-coated NPs. The doses (viz., 2.5, 5, and 10 mg L^{-1}) were chosen significantly higher than the concentrations typically used for contrast agent assisted MRI experiments. The cells were then submitted to the Alamar blue (AB) assay that tests mitochondrial activity to evaluate their cell viability. Interestingly, the cell viability was not significantly hindered at all studied concentrations. The collected data revealed for each concentration of $Co_{0.6}Zn_{0.4}Gd_xFe_{2-x}O_4$ NPs incubated with the cells, a toxicity linear with composition ($0.0 \leq x \leq 0.06$) although quite limited as viability remained always above 80% relatively to control (Fig. 12).

Additionally, confocal microscopy images were acquired on the cells incubated with the highest dose (10 mg L^{-1}) for the longest contact time (72 h). Representative immunofluorescence images (Fig. 13) recorded on cells incubated with the solid solutions and compared with those of cells not at all incubated with NPs exhibited typical fibroblast BJH morphology,

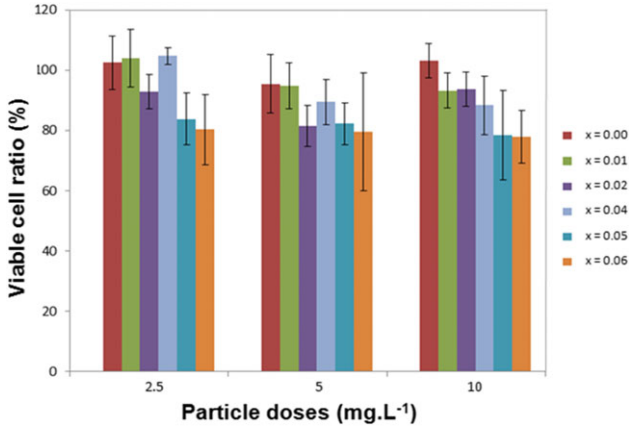

Figure 12. Number of viable human fibroblastic cells, determined by using Alamar blue test, for an exposition time of 24 h to dopamine-coated $Co_{0.6}Zn_{0.4}Fe_{2-x}Gd_xO_4$ ($0.0 \leq x \leq 0.06$) nanoparticle doses as high as 10 mg L^{-1} (expressed per mass of inorganic magnetic cores). The results are expressed as a ratio to non-stimulated serum-free cultured cells for each dose data point.

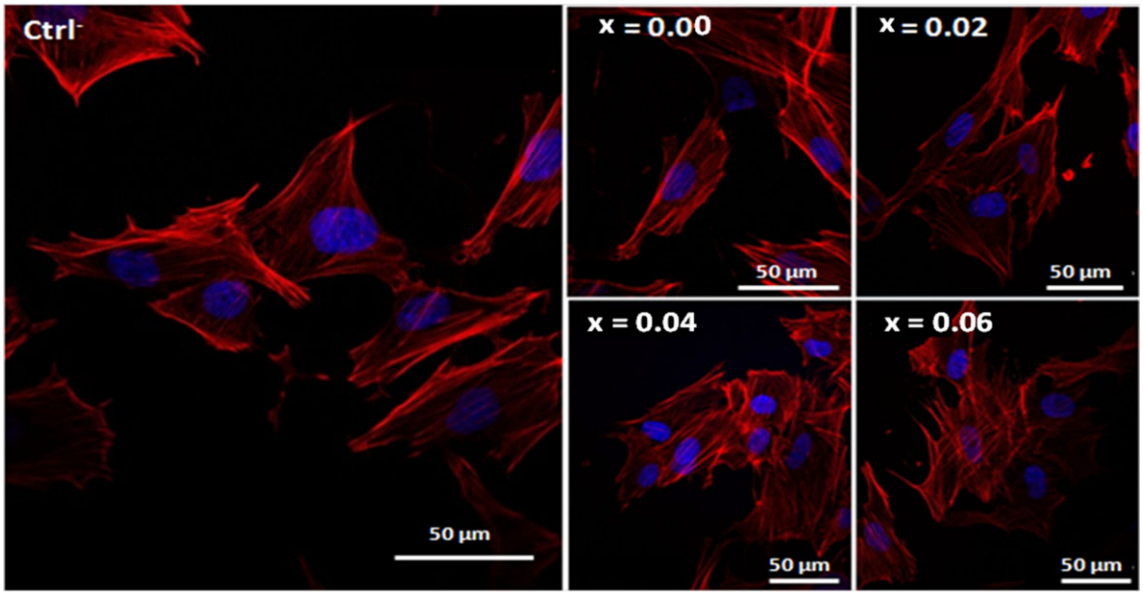

Figure 13. Confocal fluorescence microscopy images collected on BJH cells incubated during 72 h with 10 mg mL^{-1} (expressed per mass of inorganic magnetic cores) of dopamine-coated $Co_{0.6}Zn_{0.4}F_{e2-x}Gd_xO_4$ ($0.0 \leq x \leq 0.06$) nanoparticles. Please note that the nucleus and the cytoskeleton were counterstained with the blue-emitting and red-emitting DAPI and TRITC dyes, respectively.

with no change on the nuclei shape. These results are very interesting because they confirm the biosafety of the investigated NPs.

Conclusions

The influence of Gd^{3+} substitution to Fe^{3+} on the spinel structure, microstructure and magnetic properties of polyol-made nanosized $Co_{0.6}Zn_{0.4}Fe_2O_4$ particles was thoroughly investigated. A solubility limit of $x_s = 0.06$ was determined for the $Co_{0.6}Zn_{0.4}Fe_{2-x}Gd_xO_4$ solid solution with, very probably, local structural change. Far-infrared (FIR) and Raman spectroscopies suggested partial transfer of Co^{2+} cations from octahedral to tetrahedral spinel sites and reversely transfer of the same number of Fe^{3+} cations from tetrahedral to octahedral sites to relax the spinel lattice strain after large Gd^{3+} cation introduction. The produced NPs appeared as almost spherical in shape, highly crystalline, magnetic monodomains, of 5-6 nm in diameter. All the NPs exhibited superparamagnetic behavior at room temperature, with a very high saturation magnetization, close to 80 emu g^{-1} at 300 K. These high values

allow the classification of the engineered NPs in the highly magnetized ferrite-based negative MRI contrast agents. Relaxometric measurements confirmed this feature, because r_2 and r_2/r_1 values of 188 and 33 mM^{-1} sec^{-1} respectively where obtained on the DA decorated Gd-richest, limited NP clusters, dispersed in deionized water, at 37°C under a static magnetic field of 1.41 T. Besides, preliminary cytotoxicity studies carried out on healthy BHJ human fibroblast model cells incubated with doses as high as 10 mg L^{-1} of DA-coated NPs for 72 h showed a negligible cell death, likely ascribed to the Gd content, making our engineered contrast agents definitively valuable for MRI.

Experimental Section

Particle synthesis

The preparation of $Co_{0.6}Zn_{0.4}Gd_xFe_{2-x}O_4$ NPs, with a nominal *x* composition ranging between 0.0 and 0.2 by a step of 0.02, was achieved by the so-called polyol method. Analytical grade chemicals were used including iron(III) chloride hexahydrate and gadolinium(III), cobalt(II), zinc(II), and sodium(I) acetate salts. They were accurately weighed in appropriate ratios and then dissolved in 125 mL of diethyleneglycol to reach a nominal concentration of 0.2 M of total trivalent cations (Fe^{3+} and Gd^{3+}). The resulting mixture was then heated up to boiling (~220°C) and maintained under reflux for 4 h under mechanical stirring. After slow cooling, the obtained black magnetic precipitates were separated from the supernatant by centrifugation, washed with distilled water, then with ethanol, and finally dried in air at 50°C. For all the syntheses, the hydrolysis ratio, the acetate ratio, and the zinc ratio (defined as the nominal water per metal cation, acetate per metal cation, and zinc cations per trivalent cations molar ratios) were fixed to 1, 3.66, and 0.5, respectively, after a series of optimizations.

Colloidal suspension preparation

Dopamine ligand was chosen to render the produced NPs hydrophilic and water dispersible. The related hybrids were prepared according to already described operating conditions (Basti et al., 2010). In practice, 50 mg of the pre-functionalized particles were added to 3 mL of deionized water. Then, to ensure the maximum coating with the catechol derivative through an exchange chemistry of the polyol entities by DA molecules, an excess of DA was slowly added to the aforementioned mixture with assistance of ultrasonication and vortexing. Excess of acetone was then added, and a magnetic sedimentation allowed collecting the desired nanohybrids, which then became readily dispersible in water, forming very stable aqueous colloidal suspensions.

Particle characterization

The chemical compositions of the produced NPs were checked by XRF focusing on the Fe, Co, Zn, and Gd elements. The chemical compositions of the produced NPs were checked by XRF using a Epsilon 3XL (Panalytical) X-ray fluorescence spectrometer, equipped with a silver X-ray tube operating at 20 kV 200 μA. The analyses were performed on a given volume of well-concentrated aqueous solution obtained by a total acid attack of a precise mass of the as-produced particles. Fe, Co, Zn, and Gd standard and certified solutions were used for calibration. The structure of all the produced NPs was investigated by XRD using a Panalytical X'pert Pro™ instrument, equipped with a CoK_α tube (λ = 1.7889 Å). The unit cell parameter *a*, the average crystallite size $<L_{XRD}>$, and the average lattice micro-deformation $<\varepsilon>$ were inferred from Rietveld refinements, using MAUD software. Polycrystalline strain-free silicon was used as standard to estimate the instrumental XRD line broadening. To complete these structural analyses, FIR and Raman spectroscopies were performed at ambient temperature on the as-produced NPs. FIR spectra were recorded on polyethylene pellets using a Bruker Equinox Fourier transform infrared spectrometer in a transmission scheme. Raman spectra were obtained in a backscattering geometry using a LabRam HR-800 spectrometer, equipped with a 25-mW He-Ne laser source operating at 633 nm. Finally, the microstructure was determined thanks to a JEOL-100-CX II transmission electron microscope operating at 100 kV.

The magnetic properties of the as-produced NPs were determined using a Quantum Design™ MPMS-5S SQUID magnetometer. To do so, the thermal variation of the magnetic susceptibility of each sample was measured between 5 and 330 K within both FC and ZFC conditions for an applied dc-magnetic field of 200 Oe. Then, the ZFC isothermal variation of their magnetization as a function of the magnetic field was measured between +50 and −50 kOe at 5 and 300 K, dispersing first the NPs in a diamagnetic alumina (Kaiser, 99.9%) matrix (4.8 wt.%) to limit the effect of dipolar interactions on their whole magnetic behavior.

At the end, the temperature dependence of the high field (50 kOe) spontaneous magnetization was measured at different temperatures. All the data were expressed per gram of ferrite powders and corrected from the diamagnetic contribution of alumina and the sampling plastic tube.

Colloidal state characterization

The aqueous colloidal suspensions made from DA-coated NPs were also characterized. At first, the exact Fe, Co, Zn, and Gd weight contents were determined by XRF analysis using the same step-up than that described previously but working directly on the colloidal dispersions. DA grafting was checked by XPS analysis using a Thermo VG ESCALAB™ 250 instrument equipped with a micro-focused, monochromatic A1 Kα X-ray source (1.486.6 eV) and a magnetic lens. The X-ray spot size was 500 μm (15 kV, 150 W). The spectra were acquired in the constant analyzer energy mode with pass energies of 150 and 40 eV for the general survey and the narrow scans, respectively. The final DA weight content on all the prepared hybrids was determined on their dried powders by TGA, using a TA instrument™ Q50 or a Labsys-Evo™ commercial machine and heating each sample from 25°C to 800°C in air (10°C min^{-1}). The hydrodynamic diameter and the zeta potential of bare NPs, and their related DA grafted hybrids, were determined at room temperature on their aqueous suspensions (0.50 g L^{-1}) using a Malvern Nano Zetasizer operating at 90° scattering angle, after vigorous sonication with an ultrasound probe for 10 min (repeated cycles 2″ on at full power, 1″ off).

Finally, relaxometric measurements were carried out on the prepared aqueous colloids by fixing the mass of the hybrid powders around a concentration of iron close to 0.8 mM_{Fe}. The stock suspensions were diluted several times (up to height times), and ~0.7 mL of each suspension was introduced in nuclear magnetic resonance tubes (7.5-mm outer diameter). The tubes were then inserted into a Bruker Minispec™ mq60 relaxometer equipped with a 60-MHz/1.41-T magnet. The T_1 and T_2 relaxation times were recorded at 37°C, and their inverse (decay rates) were plotted as a function of the total metal ion concentrations, after subtraction of the respective decay rate in pure water. The concentrations were properly calculated by several methods and averaged together: through accurate titration of all the metallic ion content in all the samples inferred from XRF measurements; by a colorimetry assay after dissolution in HCl 5 M using the characteristic peak at 350 nm of the hexachloroferric complex (Rad et al., 2007); and finally, by TGA without any acid mineralization (leading to the total metal oxide weight). T_2 values were measured with a CPMG sequence using inter-echo times (TE) values ranging from 0.18 to 6 msec (depending on the concentration in metal centers) (Hemery et al., 2017).

Toxicity assays

In vitro cytotoxicity of the produced nanohybrids was checked by testing their effect on human fibroblastic cells cultured for 24 h. Forty-eight-well cell culture clusters (Corning, USA) were plated with 1 mL of 15,000 cells mL^{-1} cell suspension. After 24-h incubation, plates were washed with 1 mL per well phosphate buffer saline, and the cells were treated with various concentrations of particles prepared in Dulbecco's modified Eagle's medium: 2.5, 5, and 10 mg L^{-1} (corresponding to the exact inorganic magnetic core mass). The incubation was performed at 37°C in a 5% CO_2 humidified incubator for different contact times. Replicate wells were used for each control and to test the concentration in each plate. At first, AB viability assays (Al-Nasiry et al., 2007) were conducted. In practice, the cells were rinsed once with phosphate buffer saline, and 1 mL of AB medium (10% v/v solution of AB in Dulbecco's modified Eagle's medium) prepared in fresh medium was added to each well. After 3-h incubation, the AB absorbance of the samples was measured at 570 nm (A570) and 600 nm (A600) on a microplate reader. The absorbance of AB media in the absence and presence of particles was compared: no significant difference was observed, suggesting that the nanohybrids do not interact with AB or affect the assay readout. All toxicity experiments were conducted in at least triplicate (three independent experiments). Absorbance (AB assays) in optical density units was quantified using a microplate reader. Raw data from cytotoxicity assays were collated and analyzed using Microsoft Excel® (Microsoft Corporation, Redmond, WA). Cytotoxicity was expressed as the mean percentage inhibition relative to the unexposed control ± standard deviation. Statistical analyses from cytotoxicity assays were carried out using one-way analyses of variance followed by Dunnett's multiple comparison tests. Statistical significance was accepted according to Student's *t*-test at $P \leq 0.05$.

To complete these analyses, confocal microscopy was performed on the incubated cells to visualize their morphology and possibly qualitatively evaluate the NP toxicological effect. Typically, human fibroblastic cells were seeded on glass coverslips 24 h before treatment with the highest particle dose (10 mg L^{-1}) for 72 h. Fixed samples (4% paraformaldehyde) were mounted with mounting medium (Vector Laboratories, Burlingame, CA). The nuclei were counterstained with 4'6-diamidino-2-phénylindole (DAPI) (λ_{ex} = 405 nm) and the cytoskeleton with Tetramethyl-Rhodamine Iso-Thio-Cyanate (TRITC) phalloidin (λ_{ex} = 630 nm).

Acknowledgments

This work was supported by grants from the ANR (Agence Nationale de la Recherche) program "Investissements d'Avenir" Labex SEAM (ANR 11 LABX 086 and ANR 11 IDEX 05 02). The financial support from the CPER CAMPUSB project funded by the French state and the Region Nouvelle Aquitaine is also gratefully acknowledged for acquisition of the Bruker Minispec™ mq60 relaxometer. Besides, the authors want to thank Drs Philippe Decorse, Ludovic Mouton, Stéphanie Lau and Alexandre Chevillot (Paris Diderot University), and Gérard Dimier (University of Bordeaux) for their technical assistance in XPS, TEM, Raman, TGA, and relaxometry measurements. Finally, the authors want to point out that all of them contributed equally to this work.

REFERENCES

Ahmed, M. A., Ateia, E., Salah, L. M., and El-Gamal, A. A. **2005**. Structural and electrical studies on La3+ substituted Ni–Zn ferrites. Mater. Chem. Phys. *92*: 310–321.

Al-Nasiry, S., Geusens, N., Hanssens, M., Luyten, C., and Pijnenborg, R. **2007**. The use of Alamar Blue assay for quantitative analysis of viability, migration and invasion of choriocarcinoma cells. Hum. Reprod. *22*:1304–1309.

Ammar, S., Helfen, A., Jouini, N., Fiévet, F., Rosenman, I., Villain, F., Molinié, P., and Danot, M. **2001**. Magnetic properties of ultrafine cobalt ferrite particles synthesized by hydrolysis in a polyol medium. J. Mater. Chem. *11*:186–192.

Ammar, S., Jouini, N., Fiévet, F., Beji, Z., Smiri, L., Moliné, P., Danot, M., and Grenèche, J.-M. **2006**. Magnetic properties of zinc ferrite nanoparticles synthesized by hydrolysis in a polyol medium. J. Phys. Condens. Matter *18*:9055–9069.

Basti, H., Ben Tahar, L., Smiri, L. S., Herbst, F., Vaulay, M.-J., Chau, F., Ammar, S., and Benderbous, S. **2010**. Catechol derivatives-coated Fe3O4 and γ-Fe2O3 nanoparticles as potential MRI contrast agents. J. Colloid Interface Sci. *341*:248–254.

Basti, H., Hanini, A., Levy, M., Tahar, L. B., Herbst, F., Smiri, L. S., Kacem, K., Gavard, J., Wilhelm, C., Gazeau, F., Chau, F., and Ammar, S. **2014**. Size tuned polyol-made Zn0.9M0.1Fe2O4(M = Mn, Co, Ni) ferrite nanoparticles as potential heating agents for magnetic hyperthermia: from synthesis control to toxicity survey. Mater. Res. Express *1*:045047.

Beji, Z., Sun, M., Smiri, L. S., Herbst, F., Mangeney, C., and Ammar, S. **2015**. Polyol synthesis of non-stoichiometric Mn–Zn ferrite nanocrystals: structural/microstructural characterization and catalytic application. RSC Adv. *5*:65010–65022.

Bloch, F. **1930**. Zur Theorie des Ferromagnetismus. Z. Für Phys. *61*:206–219.

Bloembergen, N., and Morgan, L. O. **1961**. Proton relaxation times in paramagnetic solutions. Effects of electron spin relaxation. J. Chem. Phys. *34*:842–850.

Bregar, V. B., Lojk, J., Suštar, V., Veranič, P., and Pavlin, M. **2013**. Visualization of internalization of functionalized cobalt ferrite nanoparticles and their intracellular fate. Int. J. Nanomedicine *8*:919.

Chen, J. P., Sorensen, C. M., Klabunde, K. J., Hadjipanayis, G. C., Devlin, E., and Kostikas, A. **1996**. Size-dependent magnetic properties of $MnFe_2O_4$ fine particles synthesized by coprecipitation. Phys. Rev. B *54*:9288–9296.

Davies, K. J., Wells, S., Upadhyay, R. V., Charles, S. W., O'Grady, K., El Hilo, M., Meaz, T., and Mørup, S. **1995**. The observation of multi-axial anisotropy in ultrafine cobalt ferrite particles used in magnetic fluids. J. Magn. Magn. Mater. *149*:14–18.

Demortière, A., Panissod, P., Pichon, B. P., Pourroy, G., Guillon, D., Donnio, B., and Bégin-Colin, S. **2011**. Size-dependent properties of magnetic iron oxidenanocrystals. Nanoscale *3*:225–232.

Fouineau, J., Brymora, K., Ourry, L., Mammeri, F., Yaacoub, N., Calvayrac, F., Ammar-Merah, S., and Greneche, J.-M. **2013**. Synthesis, Mössbauer characterization, and ab initio modeling of iron oxide nanoparticles of medical interest functionalized by dopamine. J. Phys. Chem. C *117*:14295–14302.

Ghasemian, Z., Shahbazi-Gahrouei, D., and Manouchehri, S. **2015**. Cobalt Zinc Ferrite Nanoparticles as a Potential Magnetic Resonance Imaging Agent: An In vitro Study. Avicenna J. Med. Biotechnol. *7*:64.

Gilleo, M. A. **1960**. Superexchange interaction in ferrimagnetic garnets and spinels which contain randomly incomplete linkages. J. Phys. Chem. Solid *13*:33–39.

Gillis, P., Roch, A., and Brooks, R. A. **1999**. Corrected equations for susceptibility-inducedT_2-shortening. J. Magn. Reson. *137*:402–407.

Hanini, A., Lartigue, L., Gavard, J., Kacem, K., Wilhelm, C., Gazeau, F., Chau, F., and Ammar, S. **2016**. Zinc substituted ferrite nanoparticles with Zn0.9Fe2.1O4 formula used as heating agents for in vitro hyperthermia assay on glioma cells. J. Magn. Magn. Mater. *416*:315–320.

Hemery, G., Keyes, A. C., Garaio, E., Rodrigo, I., Garcia, J. A., Plazaola, F., Garanger, E., and Sandre, O. **2017**. Tuning Sizes, Morphologies, and Magnetic Properties of Monocore Versus Multicore Iron Oxide Nanoparticles through the Controlled Addition of Water in the Polyol Synthesis. Inorg. Chem. *56*:8232.

Hendriksen, P. V., Linderoth, S., and Lindgård, P.-A. **1993**. Finite-size modifications of the magnetic properties of clusters. Phys. Rev. B *48*:7259–7273.

Henoumont, C., Laurent, S., and Vander Elst, L. **2009**. How to perform accurate and reliable measurements of longitudinal and transverse relaxation times of MRI contrast media in aqueous solutions. Contrast Media Mol. Imaging *4*:312–321.

Joshi, H. M., Lin, Y. P., Aslam, M., Prasad, P. V., Schultz-Sikma, E. A., Edelman, R., Meade, T., and Dravid, V. P. **2009**. Effects of shape and size of cobalt ferrite nanostructures on their MRI contrast and thermal activation. J. Phys. Chem. C *113*:17761–17767.

Kahn, M. L., and Zhang, Z. J. **2001**. Synthesis and magnetic properties of $CoFe_2O_4$ spinel ferrite nanoparticles doped with lanthanide ions. Appl. Phys. Lett. *78*:3651–3653.

Kolekar, C. B., Kamble, P. N., and Vaingankar, A. S. **1994**. Structural and dc electrical resistivity study of $Gd3^+$-substituted Cu-Cd mixed ferrites. J. Magn. Magn. Mater. *138*:211–215.

Kreisel, J., Lucazeau, G., and Vincent, H. **1998**. Raman spectra and vibrational analysis of $BaFe_{12}O_{19}$hexagonal ferrite. J. Solid State Chem. *137*:127–137.

Kumar, P., Sharma, S., Knobel, M., Chand, J., and Singh, M. **2011**. Investigations of lanthanum doping on magnetic properties of nano cobalt ferrites. J. Electroceramics *27*:51–55.

Kumar, H., Srivastava, R. C., Pal Singh, J., Negi, P., Agrawal, H. M., Das, D., and Hwa Chae, K. **2016**. Structural and magnetic study of dysprosium substituted cobalt ferrite nanoparticles. J. Magn. Magn. Mater. *401*:16–21.

Mertz, D., Sandre, O., and Begin-Colin, S. **2017**. Drug releasing nanoplatforms activated by alternating magnetic fields. BBA: General Subjects *1861*:1617–1641.

Mørup, S., Hansen, M. F., and Frandsen, C. **2010**. Magnetic interactions between nanoparticles. Beilstein J. Nanotechnol. *1*:182–190.

Na, H. B., Song, I. C., and Hyeon, T. **2009**. Inorganic nanoparticles for MRI contrast agents. Adv. Mater. *21*:2133–2148.

Nasrazadani, S., and Raman, A. **1993**. The application of infrared spectroscopy to the study of rust systems—II. Study of cation deficiency in magnetite (Fe_3O_4) produced during its transformation to maghemite (γ-Fe_2O_3) and hematite (α-Fe_2O_3). Corros. Sci. *34*: 1355–1365.

Ngo, A. T., Bonville, P., and Pileni, M. P. **2001**. Spin canting and size effects in nanoparticles of nonstoichiometric cobalt ferrite. J. Appl. Phys. *89*:3370–3376.

Okuhata, Y. **1999**. Delivery of diagnostic agents for magnetic resonance imaging. Adv. Drug Deliv. Rev. *37*:121–137.

O'Neil, H. S. C., and Navrotsky, A. **1984**. Cation distributions and thermodynamic properties of binary spinel solid solutions. Am. Mineral. *69*:733.

Petitt, G. A., and Forester, D. W. **1971**. Mössbauer study of cobalt–zinc ferrites. Phys. Rev. B *4*:3912–3923.

Pilati, V., Cabreira Gomes, R., Gomide, G., Coppola, P., Silva, F. G., Paula, F. L. O., Perzynski, R., Goya, G. F., Aquino, R., and Depeyrot, J. **2018**. Core/shell nanoparticles of non-stoichiometric Zn–Mn and Zn–Co ferrites as thermosensitive heat sources for magnetic fluid hyperthermia. J. Phys. Chem. C *122*:3028–3038.

Rad, A. M., Janic, B., Iskander, A. S. M., Soltanian-Zadeh, H., and Arbab, A. S. **2007**. Measurement of quantity of iron in magnetically labeled cells: comparison among different UV/VIS spectrometric methods. Biotechniques *43*:627–636.

Rezlescu, E., Rezlescu, N., Popa, P. D., Rezlescu, L., and Pasnicu, C. **1997**. The influence of R_2O_3 (R = Yb, Er, Dy, Tb, Gd, Sm and Ce) on the electric and mechanical properties of a nickel–zinc ferrite. Phys. Status Solidi A *162*:673–678.

Salah, L. M. **2006**. Spectroscopic studies of the effect of addition of Y^{3+} on structural characteristics of Ni–Zn ferrites. Phys. Status Solidi A *203*:271–281.

Salunkhe, A. B., Khot, V. M., Thorat, N. D., Phadatare, M. R., Sathish, C. I., Dhawale, D. S., and Pawar, S. H. **2013**. Polyvinyl alcohol functionalized cobalt ferrite nanoparticles for biomedical applications. Appl. Surf. Sci. *264*:598–604.

Sattarahmady, N., Heidari, M., Zare, T., Lotfi, M., and Heli, H. **2016**. Zinc–nickel ferrite nanoparticles as a contrast agent in magnetic resonance imaging. Appl. Magn. Reson. *47*:925–935.

Shannon, R. D. **1976**. Revised effective ionic radii and systematic studies of interatomic distances in halides and chalcogenides. Acta Crystallogr. A *32*:751–767.

Sharifi, I., and Shokrollahi, H. **2012**. Nanostructural, magnetic and Mössbauer studies of nanosized Co1−xZnxFe2O4 synthesized by co-precipitation. J. Magn. Magn. Mater. *324*:2397–2403.

Shebanova, O. N., and Lazor, P. **2003**. Raman spectroscopic study of magnetite (FeFe2O4): a new assignment for the vibrational spectrum. J. Solid State Chem. *174*:424–430.

Shlapa, Y., Kulyk, M., Kalita, V., Polek, T., Tovstolytkin, A., Greneche, J.-M., Solopan, S., and Belous, A. **2016**. Iron-doped (La,Sr)MnO3 manganites as promising mediators of self-controlled magnetic nanohyperthermia. Nanoscale Res. Lett. *11*:24.

da Silva, S. W., Nakagomi, F., Silva, M. S., Franco, A., Garg, V. K., Oliveira, A. C., and Morais, P. C. **2010**. Effect of the Zn content in the structural and magnetic properties of $Zn_xMg_{1-x}Fe_2O_4$ mixed ferrites monitored by Raman and Mössbauer spectroscopies. J. Appl. Phys. *107*:09B503.

Solomon, I. **1955**. Relaxation processes in a system of two spins. Phys. Rev. *99*:559–565.

Spirou, S. V., Costa Lima, S. A., Bouziotis, P., Vranješ-Djurić, S., Efthimiadou, E. K., Laurenzana, A., Barbosa, A. I., Garcia-Alonso, I., Jones, C., Jankovic, D., and Gobbo, O. L. **2018**. Recommendations for in vitro and in vivo testing of magnetic nanoparticle hyperthermia combined with radiation therapy. Nanomaterials *8*:306.

Tahar, L. B., Smiri, L. S., Artus, M., Joudrier, A.-L., Herbst, F., Vaulay, M. J., Ammar, S., and Fiévet, F. **2007**. Characterization and Magnetic Properties of Sm- and Gd- Substituted $CoFe_2O_4$ Nanoparticles Prepared by Forced Hydrolysis in Polyol. Mater. Res. Bull. *42*:18886.

Tahar, L. B., Artus, M., Ammar, S., Smiri, L. S., Herbst, F., Vaulay, M.-J., Richard, V., Grenèche, J.-M., Villain, F., and Fiévet, F. **2008**. Magnetic properties of CoFe1.9RE0.1O4 nanoparticles (RE=La, Ce, Nd, Sm, Eu, Gd, Tb, Ho) prepared in polyol. J. Magn. Magn. Mater. *320*:3242–3250.

Tahar, L. B., Basti, H., Herbst, F., Smiri, L. S., Quisefit, J. P., Yaacoub, N., Grenèche, J. M., and Ammar, S. **2012**. Co1−xZnxFe2O4 ($0 \leq x \leq 1$) nanocrystalline solid solution prepared by the polyol method: characterization and magnetic properties. Mater. Res. Bull. *47*:2590–2598.

Tatarchuk, T., Bououdina, M., Macyk, W., Shyichuk, O., Paliychuk, N., Yaremiy, I., Al-Najar, B., and Pacia, M. **2017**. Structural, optical, and magnetic properties of Zn-doped $CoFe_2O_4$ nanoparticles. Nanoscale Res. Lett. *12*:141.

Valenzuela, R. **1995**. Magnetic Ceramics. Cambridge University Press, Cambridge.

Veverka, M., Veverka, P., Kaman, O., Lančok, A., Závěta, K., Pollert, E., Knížek, K., Boháček, J., Beneš, M., Kašpar, P., Duguet, E., and Vasseur, S. **2007**. Magnetic heating by cobalt ferrite nanoparticles. Nanotechnology *18*:345704.

Vuong, Q. L., Berret, J.-F., Fresnais, J., Gossuin, Y., and Sandre, O. **2012**. A universal scaling law to predict the efficiency of magnetic nanoparticles as MRI T2-contrast agents. Adv. Healthc. Mater. *1*:502–512.

Waldron, R. D. **1955**. Infrared spectra of ferrites. Phys. Rev. *99*:1727–1735.

Wáng, Y. X. J., and Idée, J.-M. **2017**. A comprehensive literatures update of clinical researches of superparamagnetic resonance iron oxide nanoparticles for magnetic resonance imaging. Quant. Imaging Med. Surg. *7*:88–122.

Wang, Z., Schiferl, D., Zhao, Y., and O'Neill, H. S. C. **2003**. High pressure Raman spectroscopy of spinel-type ferrite ZnFe2O4. J. Phys. Chem. Solid *64*:2517–2523.

White, W. B., and DeAngelis, B. A. **1967**. Interpretation of the vibrational spectra of spinels. Spectrochim. Acta Part Mol. Spectrosc. *23*:985–995.

Yan, C., Cheng, F., Liao, C., Kuang, J., Zhigang, X., Chen, L., Zhao, H., Liu, Z., Wang, Y., Zhu, T., and He,

G. **1999**. Sol–gel synthesis, magnetic and magneto-optical properties of CoFe2−xTbxO4 nanocrystalline films. J. Magn. Magn. Mater. *192*:396–402.
Yu, T., Shen, Z. X., Shi, Y., and Ding, J. **2002**. Cation migration and magnetic ordering in spinel CoFe2O4powder: micro-Raman scattering study. J. Phys. Condens. Matter *14*:L613–L618.
Zahraei, M., Monshi, A., Shahbazi-Gahrouei, D., Amirnasr, M., Behdadfar, B., and Rostami, M. **2015**. Synthesis and characterization of chitosan coated manganese zinc ferrite nanoparticles as MRI contrast agents. J. Nanostruct. *5*:77.
Zhang, D., Klabunde, K. J., Sorensen, C. M., and Hadjipanayis, G. C. **1998**. Magnetization temperature dependence in iron nanoparticles. Phys. Rev. B *58*: 14167–14170.

Supporting information

Additional supporting information may be found online in the Supporting Information section at the end of the article.

Data S1. Figure SI-1. Indexed XRD patterns of the as-produced particles for different nominal *x* compositions (from x_{nom} = 0 at the bottom to x_{nom} = 0.20 on the top by a Δx_{nom} step of 0.02).

Table SI-1. Ionic radii of octahedrally coordinated Co^{2+}, Zn^{2+}, Fe^{3+} and Gd^{3+} cations in oxides, as reported by Shannon (Ahmed et al., 2005) and refined by O'Neil et al. in spinel oxides (White and DeAngelis, 1967).

Figure SI-3. The experimental ratio of gadolinium composition to the total gadolinium and iron elements, exp-Gd/(Fe + Gd), plotted as a function of the nominal atomic gadolinium content, x_{nom}.

Table SI-2. Identification of the main bands, observed above 800 cm^{-1}, on the MIR spectra of the as-produced $Co_{0.60}Zn_{0.40}Fe_{2-x}Gd_xO_4$ nanocrystals.

Figure SI-4. Survey and high resolution C 1S, Gd $3d_{5/2}$ and N 1 s XPS spectra recorded on of the Gd richest as-produced nanoparticles (grey line) and their DA coated ones (blue line).

Figure SI-5. Thermograms of the as-produced $Co_{0.60}Zn_{0.40}Fe_{1.94}Gd_{0.06}O_4$ nanoparticles and that of their DA coated counterparts.

Figure SI-6. Zeta potential measured as a function of pH on aqueous suspension of pristine $Co_{0.60}Zn_{0.40}Fe_{1.84}Gd_{0.06}O_4$ NPs and their related DA-coated hybrids (0.5 $g{\cdot}L^{-1}$).

Figure SI-7. Relaxation rates R_1^{NP}- R_1^{water} (blue data points) and R_2^{NP}- R_2^{water} (red data points) measured on iron oxide (supposed to be close to magnetite) and cobalt ferrite nanoparticles coated by dopamine at 37°C under a magnetic field of 1.41 T. The relaxation rates of pure water have been subtracted (T_1^{water} = 3997 ms and T_2^{water} = 1020 ms) in order to obtain the relaxivity r_2 and r_2 of the NPs from the slopes of the curves.

Supporting Information

Evaluation of polyol-made Gd^{3+}-Substituted $Co_{0.6}Zn_{0.4}Fe_2O_4$ nanoparticles as high magnetisation MRI negative contrast agents.

Dr. Walid Mnasri, Prof. Lotfi Ben Tahar, Dr. Sophie Nowak, Dr. Olivier Sandre, Dr. Michel Boissière, Prof. Souad Ammar *

Physicochemical analyses of the as-produced particles

XRD patterns of all the as-produced particles were recorded (Figure SI-1) and analysed with a special emphasis on the phase purity, unit cell parameter variation and average crystal size change when the nominal Gd content is increased during the synthesis in polyol of $Co_{0.60}Zn_{0.40}Fe_{2-x}Gd_xO_4$ solid solutions. Beside, to determine the average cation-oxygen bond length of the octahedral sites into the zinc and gadolinium substituted cobalt ferrite spinel lattice, the tabulated cation radius values for Co^{2+}, Zn^{2+}, Fe^{3+} and Gd^{3+} are listed in table SI-1. Finally, the XRF spectra of selected samples of the studied solid solution are given hereafter, focusing on the Co, Zn, Fe and Gd contents in the different nanoparticles (Figure SI-2). From the inferred XRF data, the experimental gadolinium atomic ratio, $[Gd]_{exp}/[Fe+Gd]_{exp}$, is plotted as a function of the nominal Gd content, x_{nom}, in Figure SI-3 to determine the solubility limit of this element in the spinel lattice.

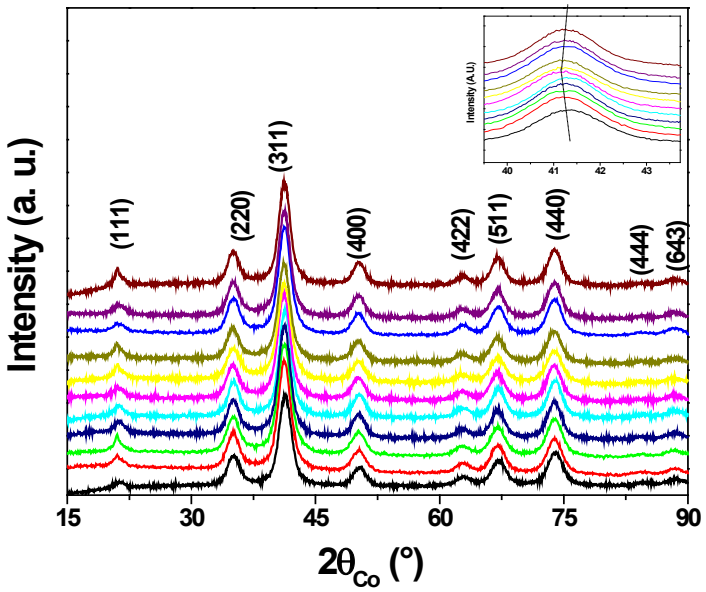

Figure SI-1. Indexed XRD patterns of the as-produced particles for different nominal x compositions (from $x_{nom} = 0$ at the bottom to $x_{nom} = 0.20$ on the top by a Δx_{nom} step of 0.02).

Cation	r (Å)
Co^{2+}	0.720
Zn^{2+}	0.742
Fe^{3+}	0.645
Gd^{3+}	0.940

Table SI-1. Ionic radii of octahedrally coordinated Co^{2+}, Zn^{2+}, Fe^{3+} and Gd^{3+} cations in oxides, as reported by Shannon [23] and refined by O'Neil *et al.* in spinel oxides [29].

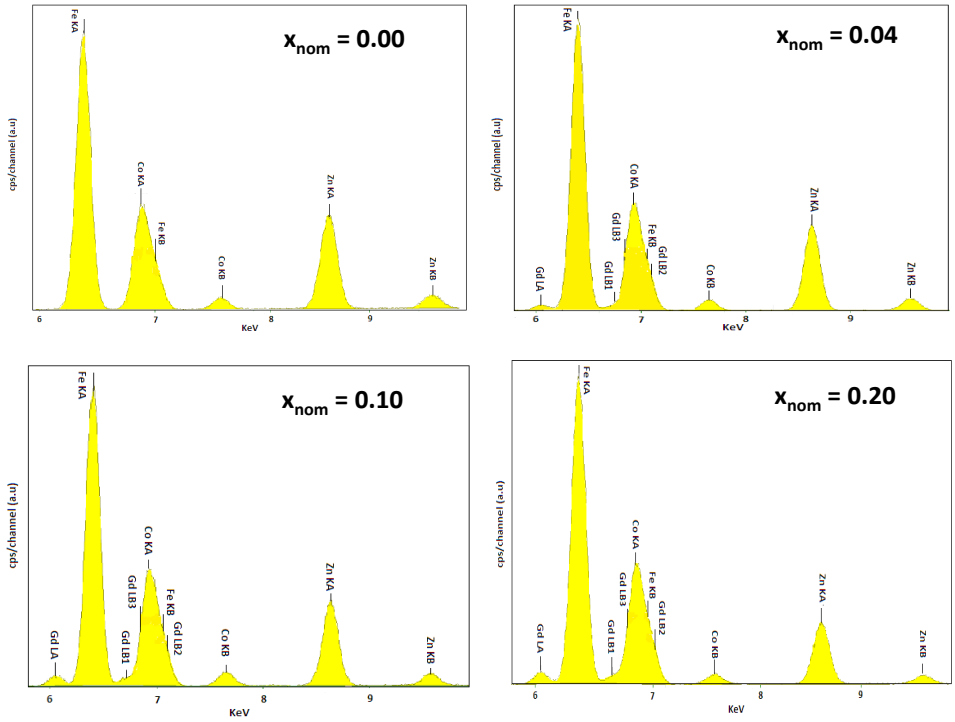

Figure SI-2. XRF spectra of some representative samples of the studied nanocrystalline $Co_{0.60}Zn_{0.40}Fe_{2-x}Gd_xO_4$ solid solutions. The constituting metallic elements were clearly identified from their respective K_α and K_β XRF peaks.

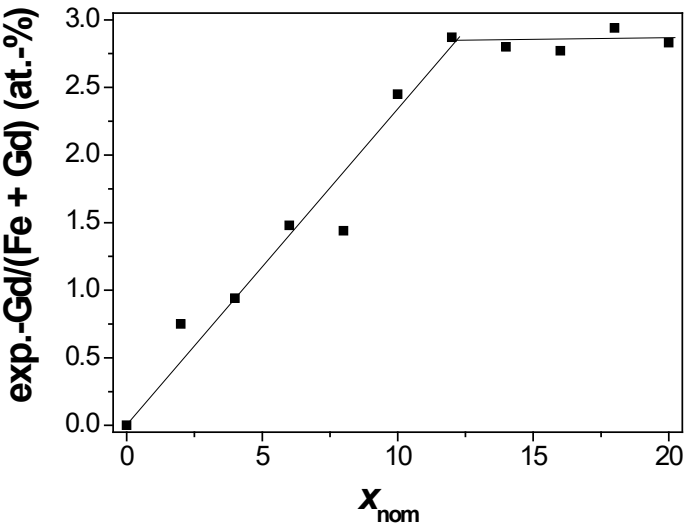

Figure SI-3. The experimental ratio of gadolinium composition to the total gadolinium and iron elements, exp-Gd/(Fe + Gd), plotted as a function of the nominal atomic gadolinium content, x_{nom}.

Finally, the mid IR (MIR) spectra of the same samples were recorded (KBr pellet technique) to characterise the as-produced nanoparticle surface state, identifying the main physi/chemisorbed organic species at their surface. The ascribing of the representative bands, observed above 800 cm^{-1}, was summarized in Table SI-2.

Wavenumber (cm^{-1})	Attribution	Adsorbing species
1150-1050	C-O-C, bridging and secondary alcohol, C-O, stretching modes of alkyl-substituted ether	Diethyleneglycol (DEG)
1407-1440	-COO symmetric stretching modes of carboxylate	Acetate
1550-1650	-COO asymmetric stretching modes of carboxylate	
2880, 2931	$-CH_x$ stretching modes of alkyls	DEG, Acetate

Table SI-2. Identification of the main bands, observed above 800 cm^{-1}, on the MIR spectra of the as-produced $Co_{0.60}Zn_{0.40}Fe_{2-x}Gd_xO_4$ nanocrystals.

Physicochemical analyses of the DA coated nanoparticles

First of all to confirm DA grafting, XPS spectroscopy was carried out on both DA coated and uncoated nanoparticles. The survey spectra as well as the high resolution ones were then compared focusing on the C1s and N1s signals, since sp^2 hybridized carbon atoms and nitrogen atoms are only present in the catechol and the amino groups carried by DA ligands, respectively. Interestingly, increasing amounts of C and N were evidenced in the functionalized nanoparticles (Fig. SI-4), in agreement with the attachment of DA onto the nanoparticle surface.

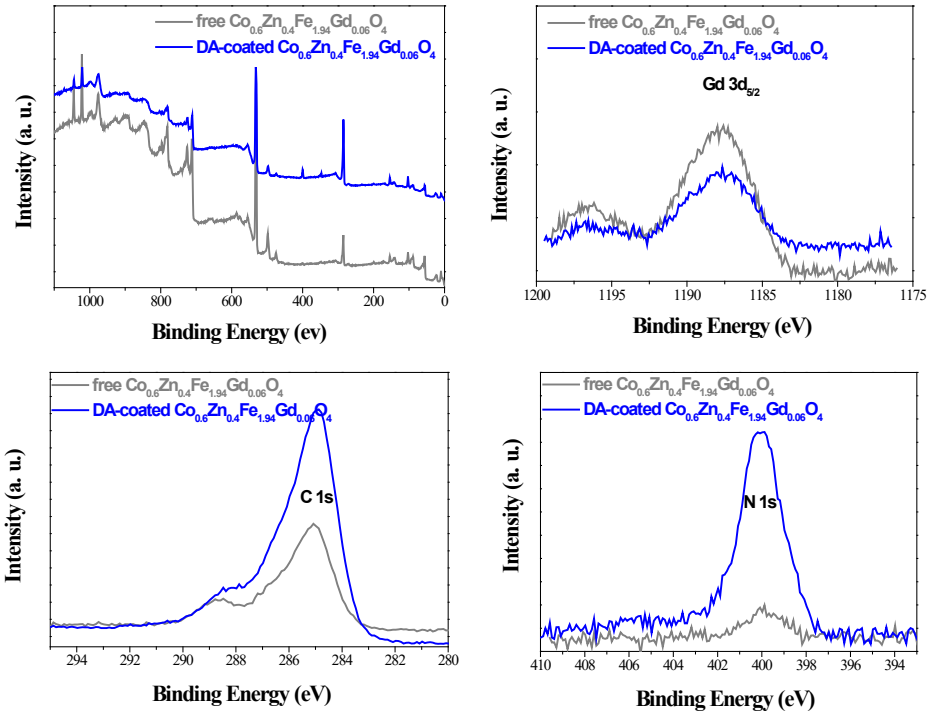

Figure SI-4. Survey and high resolution C 1S, Gd $3d_{5/2}$ and N 1s XPS spectra recorded on of the Gd richest as-produced nanoparticles (grey line) and their DA coated ones (blue line).

TG analysis was then performed, in air up to 800°C (5°C·min^{-1}) to quantify the amount of grafted DA. In practice the thermograms of the coated and uncoated nanoparticles were recorded and compared. Typically, the former exhibited two main departures, that of physisorbed water (before 100°C) and that of chemisorbed residual polyol (between 200 and 300°C). The latter exhibited a more important organic departure between 300 and 400°C, attributed to DA decomposition (Figure SI-5).

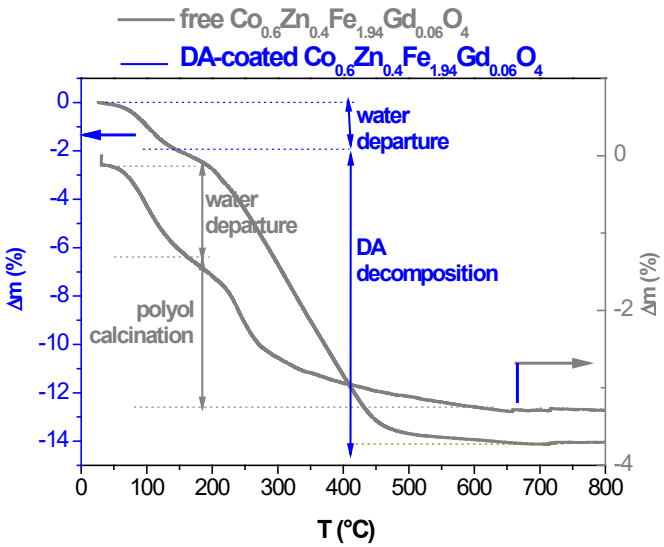

Figure SI-5. Thermograms of the as-produced $Co_{0.60}Zn_{0.40}Fe_{1.94}Gd_{0.06}O_4$ nanoparticles and that of their DA coated counterparts.

Finally, the charge surface of the formed hybrids was measured as a function of the pH and compared to that of bare $Co_{0.60}Zn_{0.40}Fe_{2-x}Gd_{0x}O_4$ particles in the following plot (Figure SI-6).

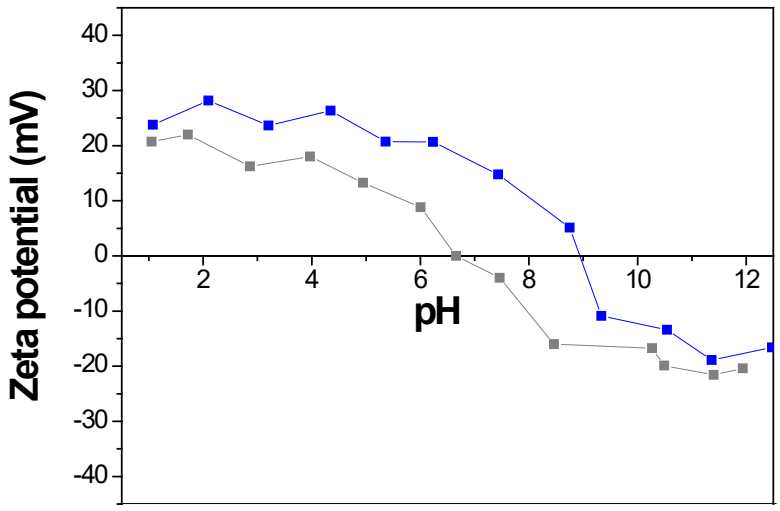

Figure SI-6. Zeta potential measured as a function of pH on aqueous suspension of pristine $Co_{0.60}Zn_{0.40}Fe_{1.84}Gd_{0.06}O_4$ NPs and their related DA-coated hybrids (0.5 g·L^{-1}).

The variation of the longitudinal and transversal relaxation rates as a function of the total metal cation concentration were plotted for the reference DA coated γ-Fe_2O_3 and $CoFe_2O_4$ nanoparticles dispersed in deionized water (Figure SI-7).

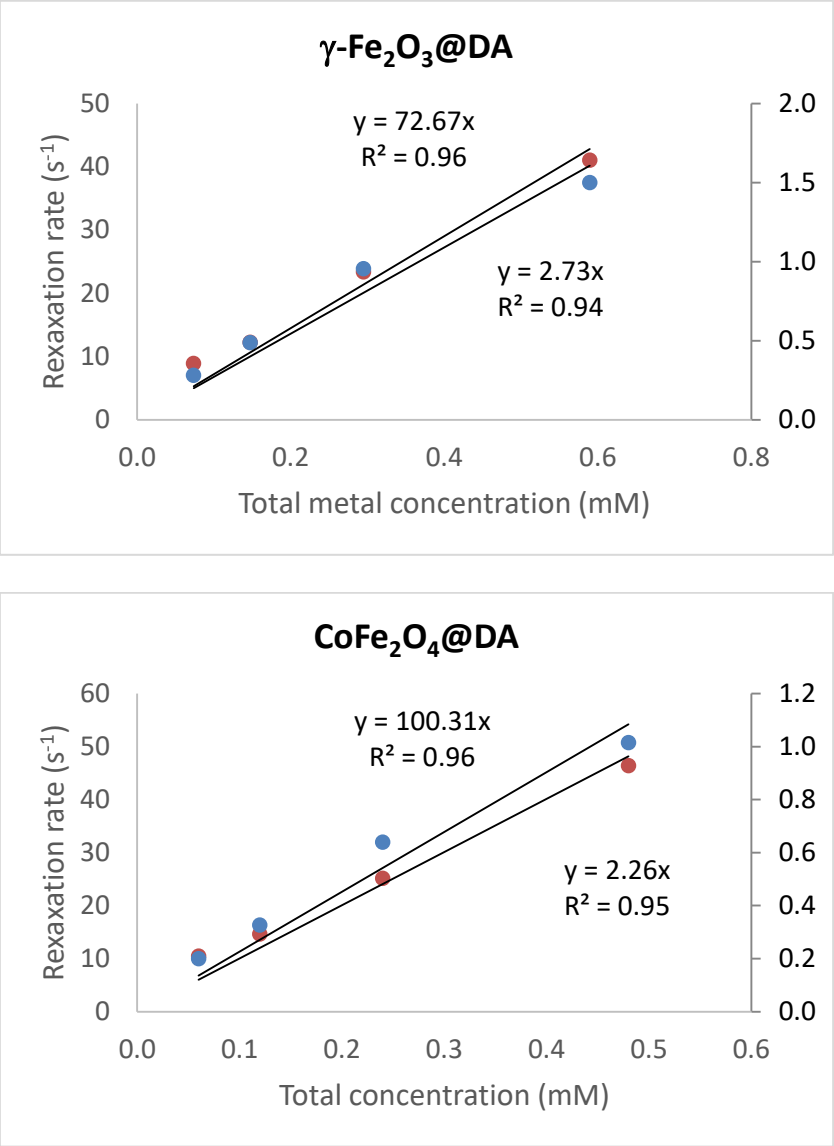

Figure SI-7. Relaxation rates $R_1^{NP} - R_1^{water}$ (blue data points) and $R_2^{NP} - R_2^{water}$ (red data points) measured on iron oxide (supposed to be close to magnetite) and cobalt ferrite nanoparticles coated by dopamine at 37°C under a magnetic field of 1.41 T. The relaxation rates of pure water have been subtracted (T_1^{water}=3997 ms and T_2^{water}=1020 ms) in order to get the relaxivity r_2 and r_2 of the NPs from the slopes of the curves.